

CRACK PROPAGATION ANALYSIS IN ELASTOMERIC ISOLATION
BEARINGS

by

Emirhan Tıknaz

B.S., Mechanical Engineering, Middle East Technical University NCC, 2017

Submitted to the Institute for Graduate Studies in
Science and Engineering in partial fulfillment of
the requirements for the degree of
Master of Science

Graduate Program in Mechanical Engineering
Boğaziçi University

2022

ACKNOWLEDGEMENTS

I would like to express my gratitude to my supervisor, Prof. Şebnem Özüpek for supporting me in any way throughout my thesis study. I wish to extend my special thanks to Arçelik Global IP team for giving me the opportunity and flexibility to complete this thesis study.

Finally, and most importantly, I am very grateful to my mother, Pembegül Gülbahar, my sister, Yasemin Mürvet Tıknaz and my father, Ahmet Tıknaz for giving me the strength, support and motivation to pursue my dreams.

ABSTRACT

CRACK PROPAGATION ANALYSIS IN ELASTOMERIC ISOLATION BEARINGS

This thesis study focuses on the crack propagation analysis in elastomeric isolation bearings. One benchmark problem related to crack propagation analysis in a single-edge notch specimen and two problems related to interface crack modelling were studied. The results such as reaction force, J integral and strain energy values were compared with the findings from literature. In the benchmark problem, conventional FEM and extended finite element method (XFEM) were used for single edge notch specimen. The strain energy values determined from conventional FEM and XFEM were in good agreement. Advantages and limitations of XFEM were investigated and it was found that J integral is not calculated in crack propagation modeling using XFEM. Therefore, a variable that would allow calculation of energy release rate was investigated. It was determined that for small crack advances, dissipated energy values obtained from the XFEM are very close to those based on J integral values calculated from FEM. 2D axisymmetric and 3D FE models of a circular elastomeric isolation bearing containing interface cracks and subjected to compression and shear loading were analyzed. For both models, the effects of fillet radius at sharp corners and coefficient of friction on the convergence of the FE analysis were investigated and optimization of these parameters to overcome convergence difficulties was accomplished. In the analysis, three different models were analyzed to improve the run time of the computation while maintaining the accuracy. J integral and reaction force for several stationary cracks were found to be in good agreement with the results obtained from the literature. In the 3D model, partial convergence was achieved for compression. For the converged combined loading the change of the J integral with the crack size followed the correct trend.

ÖZET

ELASTOMERİK İZOLASYON MESNETLERİNDE ÇATLAK İLERLEME ANALİZİ

Bu tez çalışması, elastomerik izolasyon mesnetlerinde çatlak ilerleme analizine odaklanmaktadır. Tek kenar çentikli numunede çatlak ilerleme analizi ile ilgili bir karşılaştırmalı değerlendirme problemi ve arayüz çatlak modellemesi ile ilgili iki problem incelenmiştir. Reaksiyon kuvveti, J integrali ve gerinim enerjisi değerleri gibi sonuçlar literatürden elde edilen bulgularla karşılaştırılmıştır. Değerlendirme probleminde, kenar çentikli numune için sonlu elemanlar yöntemi (FEM) ve genişletilmiş sonlu elemanlar yöntemi (XFEM) kullanılmıştır. FEM ve XFEM'den belirlenen gerinim enerjisi değerlerinin iyi bir uyumda olduğu belirlenmiştir. XFEM'in avantajları ve sınırlamaları araştırılmış ve XFEM kullanılarak yapılan çatlak ilerleme modellemesinde J integralinin hesaplanmadığı saptanmıştır. Bu nedenle enerji salınım hızının hesaplanmasına olanak sağlayacak bir değişken araştırılmıştır. Küçük çatlak ilerlemeleri için XFEM'den elde edilen enerji kaybı değerlerinin (dissipated energy due to damage) FEM'den hesaplanan J integral değerlerine çok yakın olduğu belirlenmiştir. Ara yüz çatlakları içeren ve basma ve kesme yüklerine maruz kalan silindirik elastomerik izolasyon mesnetinin 2D eksenel simetrik ve 3D sonlu eleman modelleri analiz edilmiştir. Her iki model için de keskin köşelerde köşe yarıçapının ve sürtünme katsayısının sonlu elemanlar analizinin yakınsaması üzerindeki etkileri araştırılmıştır ve yakınsama zorluklarının üstesinden gelmek için bu parametrelerin optimizasyonu gerçekleştirilmiştir. Analizde, sonuçların doğruluk derecesi değiştirilmeden çalışma süresinin iyileştirilmesi amacıyla üç farklı model analiz oluşturulmuştur. Birkaç durağan çatlak için J integrali ve tepki kuvvetinin literatürden elde edilen sonuçlarla iyi bir uyum içinde olduğu görülmüştür. 3D modelde basma için kısmi yakınsama sağlanmıştır. Basma ve kesme yüklemesi için, J integralinin çatlak boyutuyla değişimi doğru eğilimi izlemiştir.

TABLE OF CONTENTS

ACKNOWLEDGEMENTS	iii
ABSTRACT	iv
ÖZET	v
LIST OF FIGURES	ix
LIST OF TABLES	xv
LIST OF SYMBOLS	xvii
LIST OF ACRONYMS/ABBREVIATIONS	xix
1. INTRODUCTION	1
1.1. Literature Review	3
1.2. Objectives of the Thesis	6
2. THEORY AND METHODOLOGY	7
2.1. Material Behaviour of the Rubber	7
2.1.1. Large Deformation Theory	8
2.1.2. Strain Energy Potentials	9
2.2. Crack Propagation Analysis Methods	10
2.2.1. Conventional Method Based on Contour Integral (J Integral) Evaluation	10
2.2.2. Extended Finite Element Method (XFEM)	11
2.2.3. XFEM-based Cohesive Behavior	12
3. A BENCHMARK STUDY	15
3.1. Loadings and Boundary Conditions	16
3.2. Material Properties and Damage Parameters	16
3.3. Two Dimensional Model	17
3.3.1. Extended Finite Element Method (XFEM)	17
3.3.2. Conventional Finite Element Method	18
3.3.3. Results	19
3.4. Three Dimensional Model	24
3.4.1. Conventional Finite Element Method	24

3.4.2.	Extended Finite Element Method (XFEM)	25
3.4.3.	Results	27
3.4.4.	Correlation Trial between Energy Dissipated in Whole Model (XFEM) and J Integral (FEM)	28
3.4.5.	Conclusions of the Benchmark Problem	31
4.	2D CRACK MODELING IN A BEARING UNDER COMPRESSION	33
4.1.	Axisymmetric Model of the Elastomeric Bearing	33
4.2.	Finite Element Model	34
4.2.1.	Material Model	35
4.2.2.	Geometry of the Axisymmetric Model	35
4.2.3.	Mesh of the Axisymmetric Model	36
4.2.4.	Boundary Conditions and Loading	36
4.2.5.	Contact Interactions	37
4.2.6.	Geometrical Improvements of the Analytical Rigid Plate	38
4.3.	Results and Discussion	38
4.3.1.	The Effect of Fillet Radius on the Convergence of the Unbonded Bearing	40
4.3.2.	The Effects of Fillet Radius on the Convergence of the Bonded Bearing	41
4.3.3.	Interface Crack Analysis for Bonded Bearing	42
4.3.4.	Run Time (Convergence Time) Improvement	45
4.3.5.	Conclusions of the Axisymmetric Model Problem	48
5.	3D CRACK MODELING IN A BEARING UNDER COMPRESSION AND SHEAR	50
5.1.	Three Dimensional Model of the Elastomeric Bearing	50
5.1.1.	Material Model	50
5.1.2.	Geometry	50
5.1.3.	Boundary Conditions and Loading	52
5.1.4.	Contact Interactions	54
5.2.	Bearing with a Short Bondline Crack	54
5.2.1.	Mesh Structure of the Discrete Rigid Plate	54

5.2.2. Mesh Structure of the Rubber Pad	56
5.2.3. Results	57
5.3. Bearing with a Long Bondline Crack	61
5.3.1. Mesh Structure of the Discrete Rigid Plate	61
5.3.2. Mesh Structure of the Rubber Pad	62
5.3.3. Results	64
5.4. J Integral Comparison between Two Interface Cracks	67
6. CONCLUSION	70
REFERENCES	72
APPENDIX A: CONVERGENCE STUDY FOR THREE DIMENSIONAL MODEL (2.5 mm INTERFACE CRACK ANALYSIS)	75
APPENDIX B: ELSEVIER LICENSE NUMBER 5455320950504	78
APPENDIX C: ELSEVIER LICENSE NUMBER 5455540009238	79
APPENDIX D: ELSEVIER LICENSE NUMBER 5455530640334	80

LIST OF FIGURES

Figure 1.1.	Final product and configuration of high-capacity polyurethane elastomeric bearings (CPUE) [1].	1
Figure 1.2.	(a) Unbonded laminated natural bearing (b) bonded laminated natural bearing [3].	2
Figure 1.3.	(a) Internal damage caused by severe cyclic loading (b) damage due to cyclic shear displacements [4].	3
Figure 2.1.	Stress-strain curve for rubberlike materials [5].	7
Figure 2.2.	Contour for evaluation of the J-Integral [6].	11
Figure 2.3.	Linear (a) and nonlinear (b) traction-separation response [5] (T_{max} is the maximum principal stress, σ_{max} shown in the below expression).	13
Figure 3.1.	Geometry and the loading and boundary conditions applied to the body (2D model).	16
Figure 3.2.	Mesh applied on the geometry for propagating crack (XFEM).	18
Figure 3.3.	Mesh applied on the geometry for stationary crack (FEM).	19
Figure 3.4.	Crack length vs J Integral and strain energy release rate values (conventional method).	21
Figure 3.5.	Crack openings for several stationary crack lengths (conventional method) for 1 mm displacement loading magnitude.	22

Figure 3.6.	Crack openings for propagating crack (XFEM).	22
Figure 3.7.	Crack length vs strain energy values for plane-strain models.	23
Figure 3.8.	Conventional method (crack length is 0.5 m).	24
Figure 3.9.	XFEM 3D (crack length is 0.5 m).	26
Figure 3.10.	Strain energy comparison between XFEM and conventional method for 0.5 m crack.	27
Figure 3.11.	Displacement applied on the geometry vs ALLDMD value for XFEM model.	29
Figure 3.12.	J Integral difference multiplied by propagated crack length (conventional method) vs ALLDMD values obtained with XFEM model.	30
Figure 4.1.	Circular elastomeric isolation bearing.	33
Figure 4.2.	Geometry of the elastomeric rubber bearing.	34
Figure 4.3.	Geometry of the half rubber pad.	35
Figure 4.4.	Geometry of the analytical rigid plate.	36
Figure 4.5.	Mesh of the axisymmetric model.	36
Figure 4.6.	Boundary conditions, loading of the axisymmetric model and location of the interface crack.	37

Figure 4.7.	The deformed shape of the rubber subjected to 35% compression strain for bonded elastomeric isolation bearing (achieved compression strain=6.03%).	39
Figure 4.8.	The deformed shape of the rubber subjected to 35% compression strain for unbonded elastomeric bearing (achieved compression strain=3.33%).	39
Figure 4.9.	The deformed shape of the rubber subjected to 35% compression strain for unbonded elastomeric isolation bearing not containing interface crack for 0.25 coefficient of friction, 0.5 mm fillet radius (achieved compression strain=35%).	41
Figure 4.10.	The deformed shape of the rubber subjected to 35% compression loading for bonded elastomeric bearing (22.02% compression strain is achieved).	42
Figure 4.11.	The deformed shape of the bonded bearing subjected to 35% compression strain with 2.5 mm interface crack (achieved compression strain=35%).	43
Figure 4.12.	The deformed shape of the bonded bearing subjected to 35% compression strain with 15 mm interface crack (achieved compression strain=35%).	43
Figure 4.13.	Reaction force values comparison for different values of compression strains and crack lengths.	47
Figure 4.14.	J integral and tearing energy comparison for different values of compression strains and crack lengths.	48

Figure 5.1.	Geometry of the three dimensional elastomeric isolation bearing model.	51
Figure 5.2.	The geometries of the discrete rigid plates used in the 2.5 mm (left) and 15 mm stationary cracks.	52
Figure 5.3.	The geometries of the discrete rigid plates with an edge fillet used in the 2.5 mm (left) and 15 mm crack analysis.	52
Figure 5.4.	Boundary conditions and loading applied on the rubber and discrete rigid body for 2.5 mm stationary crack analysis.	53
Figure 5.5.	Boundary conditions and loading applied on the rubber and discrete rigid body for 15 mm stationary crack analysis.	53
Figure 5.6.	Mesh structure of the discrete rigid plate used for the 2.5 mm crack analysis (not containing fillet).	55
Figure 5.7.	(a) Mesh structure of the discrete rigid plate containing 0.05 mm fillet (b) mesh structure of the discrete rigid plate containing 0.1 mm fillet for the 2.5 mm crack analysis.	55
Figure 5.8.	Mesh structure of the rubber pad for 2.5 mm interface crack.	56
Figure 5.9.	Partition on the top surface of the rubber and mesh structure near the edge.	57
Figure 5.10.	Comparison of the deformed shapes: (a) deformed shape for 0.25 coefficient of friction and 0.05 mm fillet radius (0.25% compression strain is obtained) (b) deformed shape for 0.25 coefficient of friction and 0.1 mm fillet radius (10.04% compression strain is obtained).	58

Figure 5.11. Comparison of the deformed shapes: (a) deformed shape for 0.25 coefficient of friction, 0.05 mm fillet radius (10.04% compression strain is obtained) (b) deformed shape for 0.35 coefficient of friction, 0.05 mm fillet radius (15% compression and 50% shear strains are obtained). 60

Figure 5.12. Mesh structure of the discrete rigid plate for 15 mm interface crack (not containing fillet). 61

Figure 5.13. (a) Mesh structure of the discrete rigid plate containing 0.05 mm fillet (b) mesh structure of the discrete rigid plate containing 0.1 mm filled for the 15 mm crack analysis. 62

Figure 5.14. Partition on the top surface of the rubber and mesh structure on the 15 mm crack surface. 62

Figure 5.15. Mesh structure applied on the rubber for 15 mm interface crack analysis. 63

Figure 5.16. Fine mesh structure applied on the rubber for 15 mm interface crack analysis. 63

Figure 5.17. Deformed shape of the rubber pad with 15 mm crack subjected to compression and shear (coefficient of friction=0.3, fillet radius=0.05 mm and compression strain obtained=5.59%). 65

Figure 5.18. Deformed shape of the rubber pad with 15 mm crack subjected to compression and shear (coefficient of friction=0.3, fillet radius=0.1 mm and compression strain obtained=7.34%). 65

Figure 5.19.	For the fine mesh, deformed shapes of the rubber pad with 15 mm crack subjected to compression and shear for 15 mm crack analysis (coefficient of friction=0.25, fillet radius=0.1 mm and compression strain obtained=11.71%).	66
Figure 5.20.	Deformed shapes of the rubber subjected to 5% compression and 50% shear for 2.5 mm interface crack analysis (coefficient of friction=0.30 and fillet radius=0.05 mm).	67
Figure 5.21.	Deformed shapes of the rubber subjected to 5% compression and 50% shear for 15 mm interface crack analysis (coefficient of friction=0.30 and fillet radius=0.05 mm).	68
Figure 5.22.	J Integral for short bondline crack.	69
Figure 5.23.	J Integral for long bondline crack.	69
Figure A.1.	Mesh structure consisting of 5348 elements.	75
Figure A.2.	Mesh structure consisting of 134462 elements.	76
Figure A.3.	Mesh structure consisting of 10692 elements.	77
Figure A.4.	Mesh structure consisting of 8019 elements.	77
Figure B.1.	Elsevier license of Ref.[1] for Figure 1.1.	78
Figure C.1.	Elsevier license of Ref.[3] for Figure 1.2.	79
Figure D.1.	Elsevier license of Ref.[4] for Figure 1.3.	80

LIST OF TABLES

Table 3.1.	Mechanical properties of the steel	17
Table 3.2.	Damage initiation and propagation data	17
Table 3.3.	Comparison between the J Integral values and strain energy release rates determined by the conventional method (a : crack length, U : strain energy)	20
Table 3.4.	Strain energy value (ALLSE) (J) comparison between 3D and plane strain (2D) models of both XFEM and conventional FE methods for 0.5 m and 0.57 m cracks respectively(%: percentage difference, ΔU : strain energy difference between XFEM and FEM)	28
Table 3.5.	Comparison between the J Integral values and strain energy release rates determined by the conventional method (a : crack length, U : strain energy, ALLDMD: dissipated strain energy)	31
Table 4.1.	Yeoh-parameters for for natural rubber	35
Table 4.2.	Interaction properties between analytical rigid plate and crack surface	38
Table 4.3.	Coefficient of friction values between analytical rigid plate and top surface of the rubber for the unbonded bearing not containing crack and fillet versus compression obtained	40
Table 4.4.	Coefficient of friction value between analytical rigid plate and top surface of the rubber for the model not containing any crack versus compression obtained	40

Table 4.5.	Reaction force for bonded elastomeric bearing without crack	42
Table 4.6.	Reaction forces and compression strains obtained for different values of coefficient of friction for the bonded bearing with a 15 mm interface crack	44
Table 4.7.	Reaction forces and compression strains obtained for different values of fillet radii for the bonded bearing with a 15 mm interface crack .	44
Table 4.8.	Run time and J integral values for all of the models	45
Table 4.9.	Comparison of the reaction forces determined from the model with the reaction forces obtained from the literature	46
Table 4.10.	Comparison of the J Integral values determined from the model with the tearing energy values obtained from the literature	46
Table 5.1.	Interaction properties between discrete rigid plate and crack surface	54
Table 5.2.	Compression and shear strains obtained for different coefficient of friction and fillet radius values for 2.5 mm crack analysis	57
Table 5.3.	Comparison and shear strains obtained for different coefficient of friction and fillet radius values for 15 mm crack analysis	64

LIST OF SYMBOLS

b_I^α	The nodal enriched degree of freedom vector
C_{IJ}	Right Cauchy-Green deformation tensor
f	The maximum principal stress ratio
F	The deformation gradient matrix
$F_\alpha(x)$	The elastic asymptotic crack-tip functions
G_{equivC}	The equivalent fracture energy release rate
G_{equiv}	The equivalent energy release rate
G_I	The energy release rate for Mode I
G_{II}	The energy release rate for Mode II
G_{III}	The energy release rate for Mode III
$H(x)$	The discontinuous jump function across the crack surfaces
I_j	Right Cauchy-Green deformation tensor invariants
J	Determinant of the deformation gradient <i>or</i> J Integral
J^{el}	Elastic volume ratio
K	The elastic constitutive matrix
$N_I(x)$	The usual nodal shape functions
t	The nominal traction vector
t_n	The normal traction <i>or</i> the normal stress component after damage
t_s	Traction in the first shear direction <i>or</i> the shear stress component in the first shear direction after damage
t_t	Traction in the second shear direction <i>or</i> the shear stress component in the second shear direction after damage
T	Traction vector
T_n	Normal stress component without damage
T_s	Shear stress component in the first shear direction without damage

T_t	Shear stress component in the second shear direction without damage
u	Displacement vector
u_I	Usual nodal displacement
U	Strain energy potential function
W	Strain energy density
x	Final position of the material particle, Cartesian coordinate
X	Initial position of the material particle
y	Cartesian coordinate
α	Blending parameter <i>or</i> scale
$\beta_t(i)$	Backward variable
Θ	Parameter set
α	The power of the normalization
α_I	The nodal enriched degree of freedom vector
Γ	Contour surrounding the notch tip
δ_n	Separation in the normal direction
δ_s	Separation in the first shear direction
δ_t	Separation in the second shear direction
ϵ	Strain tensor
λ_j	Stretch ratios in the principle directions
$\overline{\lambda}_i$	Deviatoric stretches
μ_0	Initial shear modulus
σ	Stress tensor
σ_{max}^o	The maximum allowable principal stress
ν	Poisson's ratio

LIST OF ACRONYMS/ABBREVIATIONS

2D	Two Dimensional
3D	Three Dimensional
ALLDMD	Energy Dissipated by Damage
ALLIE	Total Strain Energy
ALLSE	Recoverable Strain Energy Stored in the Body
C3D8	An 8-Node 3-D Linear Brick Element with Full Integration
CAX8H	An 8-Node Biquadratic Axisymmetric Quadrilateral, Hybrid, Linear Pressure
C3D8RH	An 8-Node Linear Brick Element, Hybrid, Constant Pressure, Reduced Integration, Hourglass Control
CPE4	A 4-Node Bilinear Plane Strain Quadrilateral
CPUE	High-Capacity Polyurethane Elastomeric
FE	Finite Element
FEM	Finite Element Method
HDR	High Damping Rubber
LNB	Laminated Natural Rubber
NR	Natural Rubber
R3D3	A 3-Node 3-D Bilinear Rigid Triangular
R3D4	A 4-Node 3-D Bilinear Rigid Quadrilateral
XFEM	Extended Finite Element Method

1. INTRODUCTION

Laminated elastomeric isolation bearings are composites generally containing layers of rubber in between steel reinforcing shims. Their main function is to absorb the effects of seismic or external loadings and for this they are widely used for construction applications, such as hospitals, residential buildings or bridges. As illustrated in Figure 1.1 [1], they can be manufactured in various shapes having circular, rectangular [2] and profiled cross sections in accordance with the design requirements.

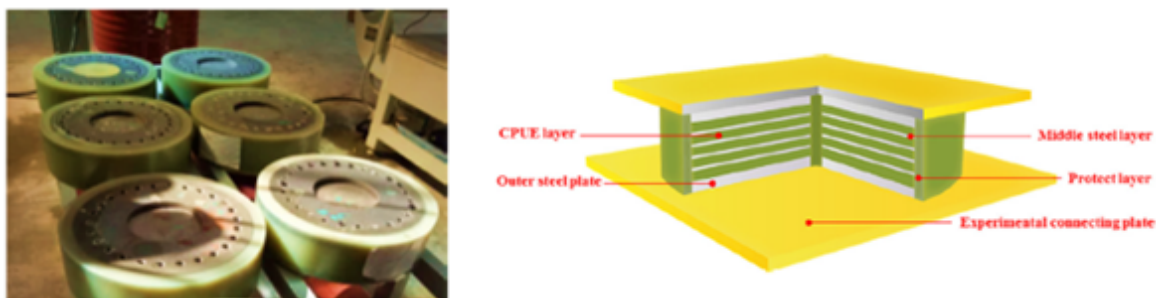


Figure 1.1. Final product and configuration of high-capacity polyurethane elastomeric bearings (CPUE) [1].

The goal of using these types of bearings is to combine flexible horizontal deformability with vertical stiffness. The isolation bearings are generally subjected to compression and cyclic shear loadings which may result in various damage such as formation of cracks in the rubber, debonding at steel-rubber interface and rupture in the shims. Growth of cracks may eventually lead to catastrophic structural failures. Motivation of this thesis is to investigate the crack modeling in selected bearing models using finite element analysis.

There are two methods to set up elastomeric bearings to the structure. One of the methods is to assemble the elastomeric bearing to the girders or cap beams via connection elements such as metric type bolts. This type of connected bearing is called bonded elastomeric bearing. If there is no connection between elastomeric bearing and girders or cap beams, it is called unbonded elastomeric bearing. Figure 1.2 [3] illustrates both bearing connection types. In this thesis, both bonded and unbonded elastomeric bearings will be modeled.

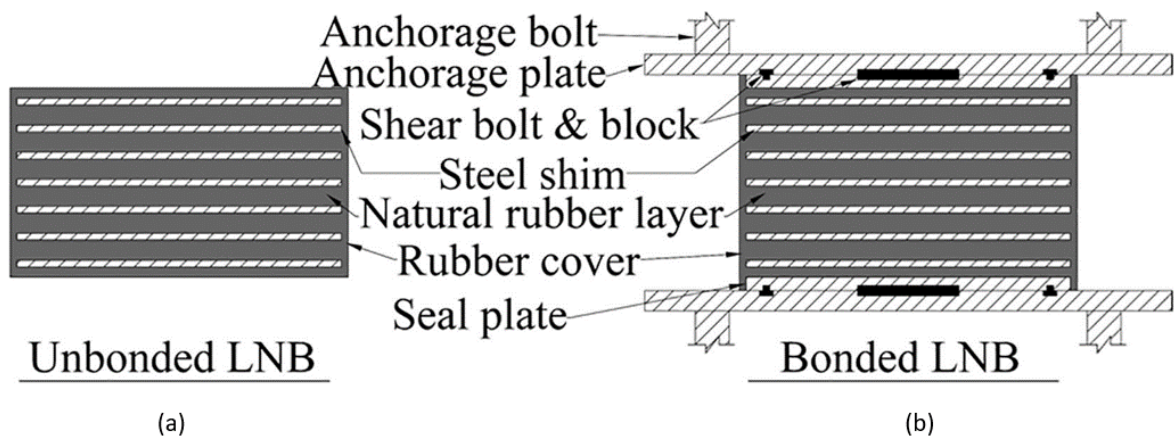


Figure 1.2. (a) Unbonded laminated natural bearing (b) bonded laminated natural bearing [3].

In particular two types of crack formation are considered. One of the problems is the occurrence of cracks in the rubber. The other problem is the tension debonding problem, that is, elastomer and bearing is separated at the end of the shims. Internal damage of elastomeric isolation bearing caused by severe cyclic loading and damage of elastomeric isolation bearing due to cyclic shear displacements are illustrated in Figure 1.3 [4]. In this model, cracks will propagate along the interface between the elastomer and the steel.

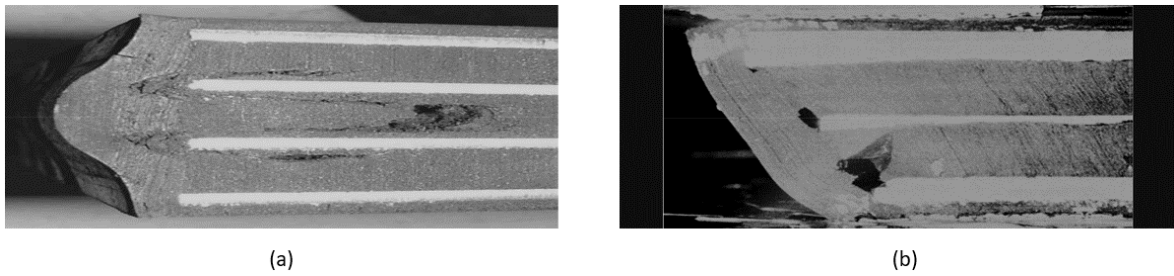


Figure 1.3. (a) Internal damage caused by severe cyclic loading (b) damage due to cyclic shear displacements [4].

1.1. Literature Review

In this section, firstly, literature review is completed for selecting the rubber material used in the elastomeric bearing subjected to compression and shear loading. Subsequently, material model parameters are selected. Additionally, the effects of compressibility of the rubber on the analysis results are considered. In regard to model cracks on the elastomeric bearings subjected to compression and shear loading, the context available in the literature is reviewed. In particular, crack locations, crack growth directions, challenges of the numerical calculations of crack propagation problems and different methods to conduct crack propagation analysis are investigated and presented in this section. The importance of using the fracture mechanics approach to predict fatigue life of the elastomeric bearing is also discussed.

A.F. Amin *et al.* [7] aimed to develop a hyperelastic material model by analyzing uniaxial compression and simple shear test data of a high damping rubber sample with rectangular cross section. Based on the test data, hyperelastic material parameters of a strain energy density function were tabulated for both rate independent instantaneous and equilibrium cases. FE analysis of the bearing subjected to compression and shear and using the obtained hyperelasticity parameters resulted in adequate accuracy.

V. Yurdabak *et al.* [8] investigated the bulk modulus effect on the solution of typical rubber problems. The goal of the study was to develop guidance for the use of explicit methods in the quasi-static analysis of nearly incompressible media with strong nonlinearities. Effects of rubber compressibility, magnitude and rate of the applied load and degree of confinement on quasi-static analysis of rubberlike materials were investigated. Comparisons of implicit and explicit integration techniques were made for two boundary value problems. One of the important conclusions was that compressibility did not have a significant effect on the accuracy of global values such as the total load. However, there is a strong dependence of the Mises stresses at stress concentration or maximum crack surface displacement on the rubber compressibility, rubber density and applied displacement.

A. Stevenson *et al.* [9] used fracture mechanics approach to predict fatigue life of profiled elastomeric bearings subjected to biaxial loading and containing internal cracks with different angles. Firstly, necessary experiments for the black filled nitrile rubber were conducted and appropriate material models were calibrated. Rubber was subjected to combined loadings of 15% compression and 75% shear. Two types of cracks, trailing edge crack and mid plane crack, were modeled. Afterwards, tearing energy as a function of crack depth was obtained. This led to more comprehension of fatigue life than the analytical approach. Final stage of the calculations was to relate depth of the selected crack as a function of loading cycle number. Crack locations and crack growth directions were discussed in particular. Some of the conclusions based on the results included that cracks near the bonded edge did not grow as it was expected and crack growth angle was the angle at which maximum value of the hoop strain was obtained.

P. Charrier *et al.* [10] compared two commercial softwares, FLEXPAC and MSC-MARC, to simulate crack propagation in elastomer components. Challenges of numerical analysis to predict the duration life of rubber components were explored. Based on the examinations regarding the challenges of the tearing energy theory such as complexity of the loading history, lack of availability of the plane strain experiment

data in the literature, difficulty of selecting the crack opening modes depending on the loading conditions, thickness effect, pre-loading effect etc., it was concluded that numerical calculations of the crack propagation problems are limited to very simple loading conditions. Additionally, the crack sizes and crack directions determined using mentioned software as a function of the number of cycles for different rubber components, were compared with the experimental data. Evaluation of the results established that crack direction is significantly affected by the loading amplitude.

H.W. Chou *et al.* [11] carried out crack initiation and crack propagation analysis of the bonded circular rubber bearings subjected to cyclic compression loading. Stress distributions in the bonded rubber cylinder were derived from Kelly's incompressibility theory, Kelly's compressibility theory and Horton's theory to calculate cracking energy. Finite element results were compare with the results obtained from the theory. It was concluded that fatigue cracks initiate at the outermost boundary between rubber and steel plates and propagate towards the center of the circular rubber bearings.

H.W. Chou *et al.* [12] studied fatigue life prediction for circular rubber bearings subjected to cyclic compression loading. Both numerical and theoretical analyses were performed. Energy release rate depending on both cracking energy density and crack length along the predicted crack propagation path was theoretically obtained at any location in the rubber. The effects of thermal aging, fatigue parameters of three different rubber compounds, intrinsic flaw and maximum compressive stress on fatigue life of the elastomeric bearing were investigated and found to be significantly important. Four different regimes of crack growth rates of elastomer with respect to different energy release rates were schematically shown and explained. First regime is the region in which crack growth rate (cm/number of cycle) is constant while energy release rate is constantly increasing. It was concluded that extension of the first regime results in more fatigue resistive circular elastomeric bearings, that is, more number of cycles could be applied on the elastomeric bearing until catastrophic structural failure.

Ş. Özüpek *et al.* [13] studied simulation of cracks in finitely deforming nonlinear viscoelastic material subjected to thermal loading. The object of this study was to establish a computational methodology for crack propagation analysis in bulk material and interface debonding. For bore cracking due to cyclic temperature, extended finite element method was used. For the propagation of initial debonding, cohesive zone modelling was used. Two benchmark problems, which are a linear elastic plate with a single edge crack and a linear viscoelastic plate with a double-edge crack, were analyzed. Conclusions were made such that crack propagation arises during the first cooldown and the relationship between crack growth and initial crack size is parabolic. It was also stated that extended finite element method and cohesive zone modelling are appropriate methods for crack propagation analysis for these benchmark problems.

1.2. Objectives of the Thesis

Main focus of this thesis is the use of fracture mechanics approach based on computational techniques to predict fatigue life of elastomeric bearings. One of the objectives of this thesis is to investigate two different crack propagation analysis methods which are the conventional method based on the calculation of a contour integral, and the extended finite element methods (XFEM). The other objective is to analyze propagation of cracks in a circular bearing along the interface of the elastomer and the steel. In order to accomplish these objectives, firstly, a benchmark problem is studied in Chapter 3. Advantages and shortcomings of the conventional finite element method and XFEM are stated by comparing the J integral results. In Chapter 4, axisymmetric model for cylindrical elastomeric bearings subjected to compression loading is completed. Several interface cracks are modeled and results are compared with the data in the literature. Finally, in Chapter 5, straight interface cracks for three dimensional cylindrical elastomeric bearing subjected to compression and shear loading are modeled and the results are compared with the literature.

2. THEORY AND METHODOLOGY

In this section, material behaviour and compressibility of the rubber are explained. Afterwards, large deformation theory and crack propagation analysis methods are introduced.

2.1. Material Behaviour of the Rubber

Rubber behaves as a hyperelastic material, that is, it has an elastic response and undergoes large deformations mostly over 100% strain values. Typical stress strain curve of a rubber-like material is shown in Figure 2.1 [5]. It is also important to state that often hyperelastic material model for rubber is assumed to be isotropic.

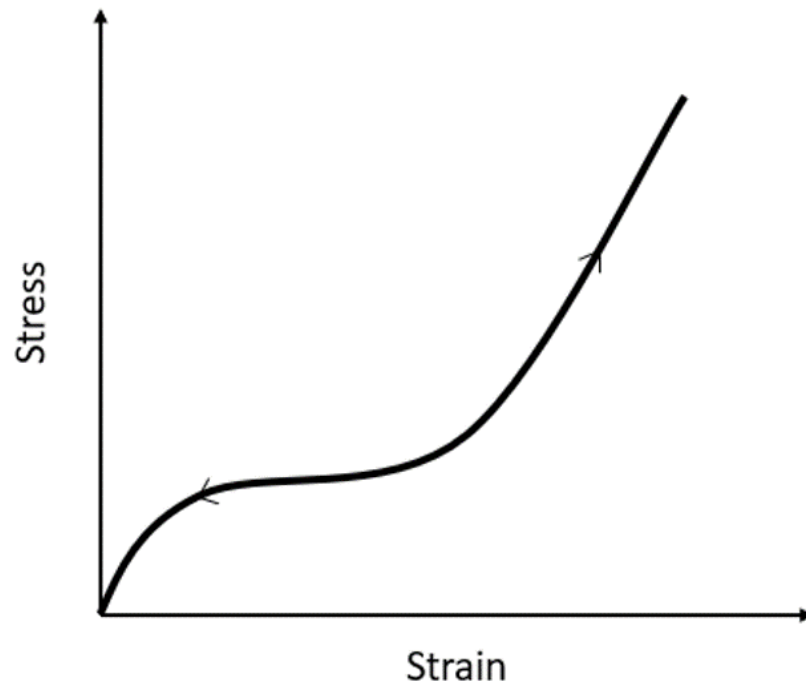


Figure 2.1. Stress-strain curve for rubberlike materials [5].

2.1.1. Large Deformation Theory

Throughout this study, elastomeric rubber bearings are subjected to large compression and/or shear strains. Therefore, in this subsection, the large deformation theory is summarized.

When a material particle is at its initial position, \mathbf{X} , and after a certain time period it is in a new position, \mathbf{x} , the relationship can be expressed in component form as

$$x = x(X, t). \quad (2.1)$$

This relationship can be extended to the following equation as

$$dx = \frac{\partial x}{\partial X} \cdot dX. \quad (2.2)$$

The gradient part of Equation 2.2 is the deformation gradient matrix and can also be expressed as

$$\mathbf{F} = \begin{bmatrix} \frac{\partial x_1}{\partial X_1} & \frac{\partial x_1}{\partial X_2} & \frac{\partial x_1}{\partial X_3} \\ \frac{\partial x_2}{\partial X_1} & \frac{\partial x_2}{\partial X_2} & \frac{\partial x_2}{\partial X_3} \\ \frac{\partial x_3}{\partial X_1} & \frac{\partial x_3}{\partial X_2} & \frac{\partial x_3}{\partial X_3} \end{bmatrix}. \quad (2.3)$$

Based on the deformation gradient, Right Cauchy-Green deformation tensor is defined as

$$C_{IJ} = F_{kI}F_{kJ} = \frac{\partial x_k}{\partial X_I} \frac{\partial x_k}{\partial X_J}. \quad (2.4)$$

Right Cauchy-Green deformation tensor has a significant role in deriving the isotropic hyperelastic material response as its invariants are variables used in strain energy functions. Invariants can be also expressed by using the stretch ratios as

$$\lambda_j = \frac{\partial x_j}{\partial X_j}, \quad (2.5)$$

where λ_1 , λ_2 and λ_3 are the ratios in the deformed length to the undeformed length in the principal directions.

Right Cauchy-Green deformation tensor invariants are:

$$I_1 = \lambda_1^2 + \lambda_2^2 + \lambda_3^2, \quad (2.6)$$

$$I_2 = \lambda_1^2\lambda_2^2 + \lambda_2^2\lambda_3^2 + \lambda_3^2\lambda_1^2, \quad (2.7)$$

$$I_3 = \lambda_1^2\lambda_2^2\lambda_3^2. \quad (2.8)$$

There are two parts of strain-energy function: volumetric and deviatoric parts. Deviatoric strain energy function is for expressing the shape changes at constant volume. Rubber-like materials are nearly incompressible or assumed to be incompressible. Therefore, they undergo very small volumetric changes upon loading. Therefore, for accuracy of the strain energy calculations, the strain energy functions in terms of volume preserving stretch ratios ($\bar{\lambda}_i$) can be expressed as

$$\bar{\lambda}_i = J^{-1/3}\lambda_i. \quad (2.9)$$

J is the determinant of the deformation gradient and can be expressed as

$$J = \det(F). \quad (2.10)$$

2.1.2. Strain Energy Potentials

Strain energy potential functions are used to describe the behavior of the hyper-elastic material. Strain energy density is defined as the energy stored in the material per unit volume as a function of strain. Some of the strain energy potential functions used in ABAQUS are Arruda-Boyce form, the Marlow form, the Mooney-Rivlin form, the neo-Hookean form, the Ogden form, the polynomial form, the Yeoh form, and the Van der Waals form. Depending on the experimental data gathered from the literature, one of the forms that describes the behavior best is used while modelling the rubber and model parameters are calibrated using test data. In representing the behavior of the rubber, Yeoh hyper-elastic elastic model performs better in terms of computational efficiency, accuracy and test data needed for calibration of the model, as shown for example by Marcin Gajewski *et al.* [14].

Yeoh strain energy potential function can be written as

$$U = C_{10}(\bar{I}_1 - 3) + C_{20}(\bar{I}_1 - 3)^2 + C_{30}(\bar{I}_1 - 3)^3 + \frac{1}{D_1}(J^{el} - 1)^2 + \frac{1}{D_2}(J^{el} - 1)^4 + \frac{1}{D_3}(J^{el} - 1)^6, \quad (2.11)$$

where U is the strain energy per unit of reference volume, C_{10} , C_{20} , C_{30} and D_1 , are the parameters that may depend on temperature and as explained above, J^{el} is the elastic volume ratio and \bar{I}_1 is the deviatoric strain invariant and is given as

$$\bar{I}_1 = \bar{\lambda}_1^2 + \bar{\lambda}_2^2 + \bar{\lambda}_3^2. \quad (2.12)$$

The initial shear modulus and initial bulk modulus are given as

$$\mu_0 = 2C_{10}, \quad (2.13)$$

$$K_0 = \frac{2}{D_1}. \quad (2.14)$$

In this thesis rubber material of the isolation bearing is modeled with Yeoh model and filled natural rubber is used as the rubber material.

2.2. Crack Propagation Analysis Methods

In this section, the crack propagation computational techniques used in this thesis are briefly described.

2.2.1. Conventional Method Based on Contour Integral (J Integral) Evaluation

An important variable used to measure growth of a crack is the strain energy release rate. It is the decrease of the strain energy value per unit area (fracture surface) due to singularities such as cracks in the material. The energy required for the crack to grow is causing this reduction in the strain energy. Another important variable is the J-integral which is a path independent integral calculated using a contour around a crack tip. According to Rice [15], J integral and energy release rate are equal under quasi-static conditions for the linear elastic materials. Additionally, their values are

equal for the materials that experience small plastic deformation at the crack tip. In Figure 2.2, linear elastic material having a crack, contour around the crack tip, normal vector to the contour and coordinate directions are shown.

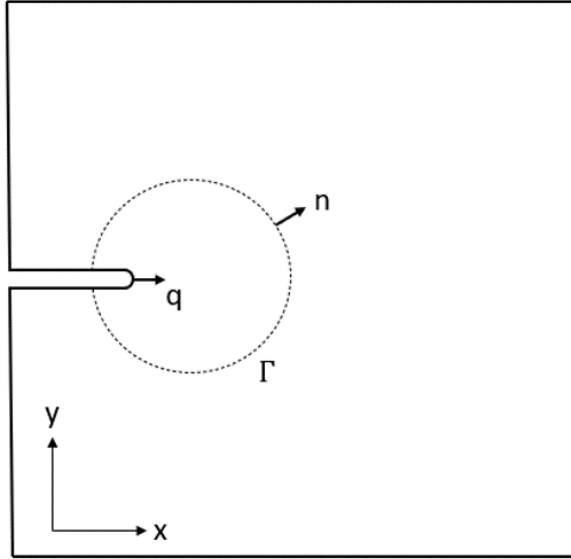


Figure 2.2. Contour for evaluation of the J-Integral [6].

In Rice's article [15], J integral and the strain energy density are given as

$$J = \int_{\Gamma} \left(W_s dy - \mathbf{T} \cdot \frac{\partial \mathbf{u}}{\partial \mathbf{n}} \right), \quad (2.15)$$

$$W = \int_0^{\epsilon} \boldsymbol{\sigma} d\boldsymbol{\epsilon}, \quad (2.16)$$

where J stands for the J integral, Γ is a contour surrounding the notch tip, x and y are the Cartesian coordinates, \mathbf{u} is the displacement vector, \mathbf{T} is the traction vector, W is the strain energy density, $\boldsymbol{\epsilon}$ is the strain tensor, $\boldsymbol{\sigma}$ is the stress tensor.

2.2.2. Extended Finite Element Method (XFEM)

Conventional crack modelling methods using finite element analysis only allow crack to propagate along element interface. As crack grows remeshing is required. XFEM overcomes the need for remeshing since crack may propagate through elements.

XFEM uses additional functions together with the piecewise polynomial functions used in the finite element method (FEM). These additional functions are called enrichment functions and Heaviside and crack tip asymptotic functions. While Heaviside functions represent the displacement jump across the crack face, crack tip asymptotic functions model the singularity at the crack tip [5]. XFEM displacement interpolation is expressed as

$$u^h(x) = \sum_{I \in N} N_I(x) \left[\mathbf{u}_I + H(x)\boldsymbol{\alpha}_I + \sum_{\alpha=1}^4 F_\alpha(x)\mathbf{b}_I^\alpha \right], \quad (2.17)$$

where $N_I(x)$ are the usual nodal shape functions, \mathbf{u}_I is the usual nodal displacement vector, $\boldsymbol{\alpha}_I$ is the nodal enriched degree of freedom vector, $H(x)$ is the discontinuous jump function across the crack surfaces, \mathbf{b}_I^α is the nodal enriched degree of freedom vector, $F_\alpha(x)$ is the elastic asymptotic crack-tip functions [5]-[16].

2.2.3. XFEM-based Cohesive Behavior

Cohesive behavior models for the separation of two surfaces. In this method, it is assumed that the traction-separation relation is initially linear. Afterwards, the initiation and evaluation of the damage is predicted. The normal and shear stresses and, the normal and shear separations, respectively of a cracked element are related by the elastic constitutive matrix. Thus, the elastic behavior is represented as

$$\mathbf{t} = \begin{Bmatrix} t_n \\ t_s \\ t_t \end{Bmatrix} = \begin{bmatrix} K_{nn} & 0 & 0 \\ 0 & K_{ss} & 0 \\ 0 & 0 & K_{tt} \end{bmatrix} \begin{Bmatrix} \delta_n \\ \delta_s \\ \delta_t \end{Bmatrix} = \mathbf{K}\boldsymbol{\delta}, \quad (2.18)$$

where \mathbf{t} is the nominal traction vector, \mathbf{K} is the elastic constitutive matrix, t_n is the normal traction, t_s and t_t are the two shear tractions. The separations are, δ_n , δ_s and δ_t if the model is three dimensional. The terms, K_{nn} , K_{ss} and K_{tt} are determined depending on the elastic properties for an enrichment element. Linear and nonlinear traction-separation responses are shown in Figure 2.3 [5].

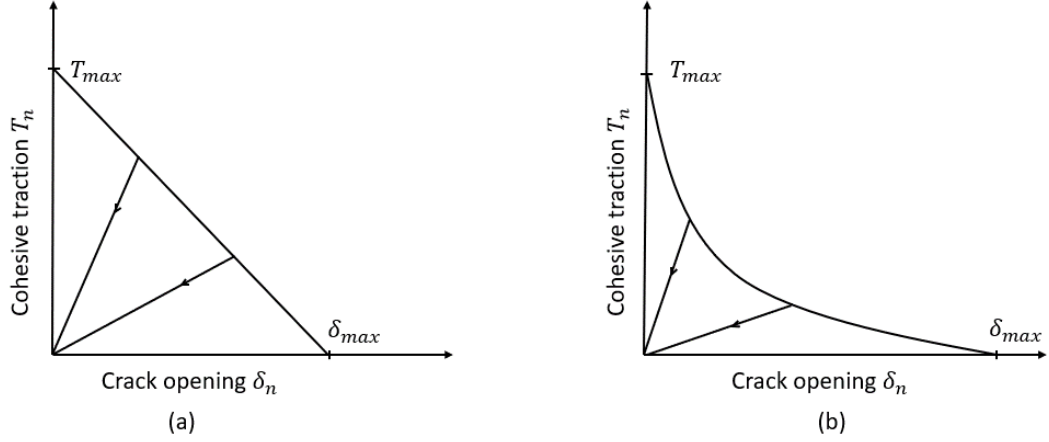


Figure 2.3. Linear (a) and nonlinear (b) traction-separation response [5] (T_{max} is the maximum principal stress, σ_{max} shown in the below expression).

Maximum principal stress damage initiation criterion expressed as

$$f = \left\{ \frac{\langle \sigma_{max} \rangle}{\sigma_{max}^o} \right\}, \quad (2.19)$$

is commonly selected. In this expression, σ_{max}^o , is the maximum allowable principal stress, $\langle \rangle$ symbol is for representing the Macaulay bracket which stands for $\langle \sigma_{max} \rangle = 0$ if $\sigma_{max} < 0$ and $\langle \sigma_{max} \rangle = \sigma_{max}$ if $\sigma_{max} \geq 0$ and f is the maximum principal stress ratio. In this criterion, damage initiates when the principal stress ratio, which is a scalar variable, f , reaches to a value of one. After damage is initiated, damage evaluation law, describes the rate at which the cohesive stiffness is degraded. Averaged overall damage at the intersection between the crack surfaces and the edges of cracked elements is defined by a scalar damage variable, D , which is stated in the following expressions as

$$t_n = \begin{cases} (1 - D)T_n, & T_n \geq 0 \\ T_n, & T_n < 0 \text{ no damage to compressive stiffness,} \end{cases} \quad (2.20)$$

$$t_s = (1 - D)T_s, \quad (2.21)$$

$$t_t = (1 - D)T_t, \quad (2.22)$$

where T_n , T_s and T_t are the normal and shear stress components, respectively without damage, t_n , t_s and t_t are the normal and shear stress components, respectively after the damage [5].

In practice, more than one crack opening modes are combined with each other. One of the most common failure criterion for mixed-mode interface crack propagation is the power law criterion [17]. In the power law model, critical energy release rates of each mode are used to normalize energy release rates of each mode as it is shown as

$$\frac{G_{equiv}}{G_{equivC}} = \left(\frac{G_I}{G_{IC}} \right)^\alpha + \left(\frac{G_{II}}{G_{IIC}} \right)^\alpha + \left(\frac{G_{III}}{G_{IIIC}} \right)^\alpha, \quad (2.23)$$

where G_{equivC} is the equivalent fracture energy release rate, G_{equiv} is the equivalent energy release rate, G_I is the energy release rate for Mode I, G_{II} is the energy release rate for Mode II, G_{III} is the energy release rate for Mode III, α is the power of these normalization. Power law criterion states that if the equivalent fracture energy release rate equals to the equivalent energy release rate, fracture occurs. When the value of α is equal to 1, linear relationship between critical energy release rate components is constructed which is a conservative assumption [18]. According to the test results α lies in between 1 and 2 depending on the material [17].

3. A BENCHMARK STUDY

In this benchmark study, crack propagation analysis of a single-edge notch specimen is completed. Since one of the objectives in this thesis is to employ XFEM in crack propagation simulation, in the benchmark study

- Capabilities of the XFEM to model crack propagation are evaluated.
- The strain energy values determined from XFEM and conventional FEM are compared.

For this purpose, both XFEM model for a propagating crack and conventional FE model for several stationary cracks along a predetermined path are used. For both XFEM and FEM, two dimensional and three dimensional models are constructed. Traction-separation damage model described in Section 2.2.3 is used for the XFEM. In the XFEM analysis, it is realized that J integral cannot be requested for a propagating crack. Therefore, a variable that would allow calculation of energy release rate is investigated. First, the strain energy values are determined from XFEM and conventional FEM for two dimensional and three dimensional models.

For two dimensional model, J integral values and strain energy release rate values determined by conventional FEM, are compared.

Then, change in the strain energy between two cracks, that is the energy release rate, are calculated for two dimensional and three dimensional models. Finally, a correlation study for a variable available in XFEM that would allow calculation of energy release rate is conducted.

3.1. Loadings and Boundary Conditions

Single edge notch specimen whose geometry is shown in Figure 3.1 is subjected to uniaxial tension. 0.3 m initial crack is located at the symmetry plane. The load is applied as displacement with a magnitude of 1 mm on the upper and lower surface of the body.

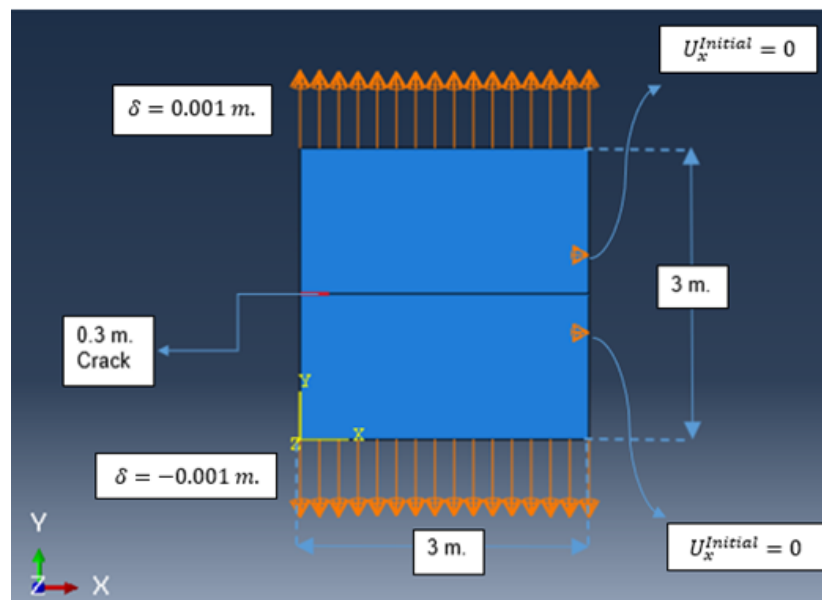


Figure 3.1. Geometry and the loading and boundary conditions applied to the body (2D model).

3.2. Material Properties and Damage Parameters

The material of the plate whose mechanical properties are tabulated in Table 3.1 is selected as linear elastic in this benchmark problem.

For traction-separation model, damage initiation is determined by maximum principal stress failure criterion given in Equation 2.19, that is, crack starts propagating when the maximum principal stress value of 220 MPa is reached.

Table 3.1. Mechanical properties of the steel.

Elastic Modulus (E) (GPa)	Poisson's Ratio (ν)
210	0.3

For the damage propagation, energy-based damage evolution law based on a power law criterion given in Equation 2.23 is used. The relevant damage initiation and propagation data is shown in Table 3.2 [5].

Table 3.2. Damage initiation and propagation data.

Maximum Principal Stress (MPa)	Critical Energy Release Rate (N/m^2)	Power Law Criterion
σ_{max}	$G_{IC}, G_{IIC}, G_{IIIC}$	α
220	42200	1

3.3. Two Dimensional Model

3.3.1. Extended Finite Element Method (XFEM)

Cracks modeled as an enriched feature is generally referred to as the XFEM crack. An XFEM crack is represented in terms of nodal values of a level set function. The crack tip/front and the virtual crack extension direction are predicted by the level set signed distance functions. To be able to define extended finite element crack, enriched region is defined. The crack will be initiated and propagated in the enriched region. Partitioning on the geometry to define the crack and crack tip or crack front is not needed as XFEM cracks initiate and propagate automatically according to the specified damage parameters. There is no need for re-meshing on the geometry, therefore the same mesh is used throughout the XFEM analysis [5].

For the extended finite element crack analysis, 4-node bilinear plane strain quadrilateral (CPE4) element type is used. The number of elements and number of nodes in the model are 1161 and 1233 respectively. Finite element mesh used in the analysis is shown in Figure 3.2.

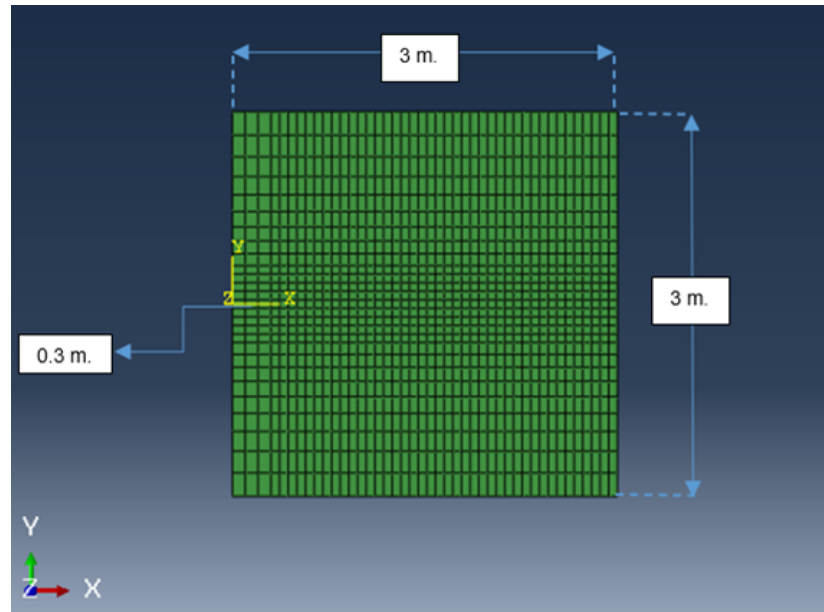


Figure 3.2. Mesh applied on the geometry for propagating crack (XFEM).

3.3.2. Conventional Finite Element Method

For the finite element analysis, 4-node bilinear plane strain quadrilateral (CPE4) element type is used. The mesh shown in Figure 3.3 consists of 3600 and 3730 elements and nodes respectively. An initial crack of 0.3 m is created. To grow the crack, a new mesh is created with a longer crack. The element and node numbers for different cracks remained the same. As the geometry and the loading shown in Figure 3.1 are symmetric, the crack is expected to propagate parallel to the x axis.

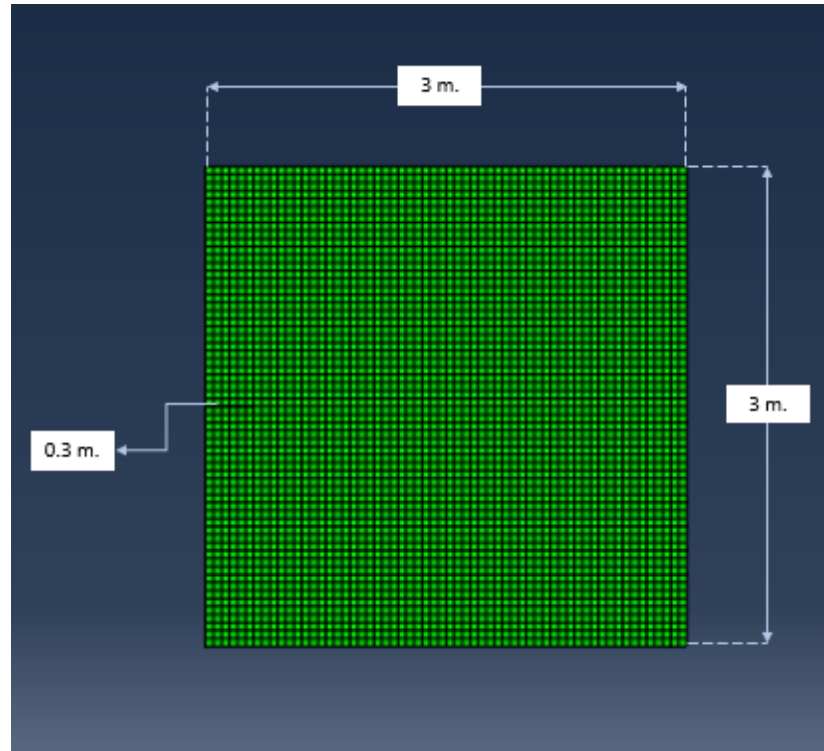


Figure 3.3. Mesh applied on the geometry for stationary crack (FEM).

3.3.3. Results

In this section, J integral values and strain energy release rate values are compared for several stationary cracks. Afterwards, Von Mises stresses around the crack tip are compared for several stationary cracks. Finally, strain energy values obtain from XFEM and FEM analysis are compared and the results are presented.

J integral values are compared to the strain energy changes ΔU per crack advance Δa for conventional FE analysis. As it is explained previously, J integral and energy release rate are equal under quasi-static conditions for the linear elastic materials. This expression is shown as

$$J = \frac{U_2 - U_1}{a_2 - a_1} = \frac{\Delta U}{\Delta a}, \quad (3.1)$$

where U_1 , is the initial total strain energy, U_2 , is the final total strain energy, ΔU , is

the change in total strain energy, a_1 , is the initial crack length, a_2 , is the final crack length and Δa is the change in the crack lengths. Strain energy release rates and J Integral values obtained from FEM analysis for several stationary cracks are tabulated in Table 3.3 and plotted in Figure 3.4. As it can be seen in Figure 3.4 and Table 3.3, J integral values are sufficiently close to the energy release rates for all crack lengths. For small crack advances, e.g., $\Delta a=0.065$ m, the agreement is better. When Δa is large, e.g. 0.43 m, discrepancy between J integral and energy release rate values occurs.

Table 3.3. Comparison between the J Integral values and strain energy release rates determined by the conventional method (a : crack length, U : strain energy).

a (m)	Δa (m)	U (J)	ΔU (J)	$\frac{\Delta U}{\Delta a}$ (J/m ²)	J Integral (J/m ²)
0.3	0.135	176807	6283	46542	39458
0.435	0.065	170524	3457	53196	51568
0.5	0.07	167066	3930	56155	56681
0.57	0.43	163135	25857	60133	57456
1	0.5	137278	26743	53486	60672
1.5	-	110535	-	-	62237

In the XFEM analysis, time step data is obtained once propagating crack (XFEM crack) reaches to the stationary crack lengths (a). In the FEM analysis, the values regarding the J integral and strain energy shown in Table 3.3 are taken at the same time step. The reason of this is to be able to compare the strain energy results obtained from stationary and propagating crack analysis.

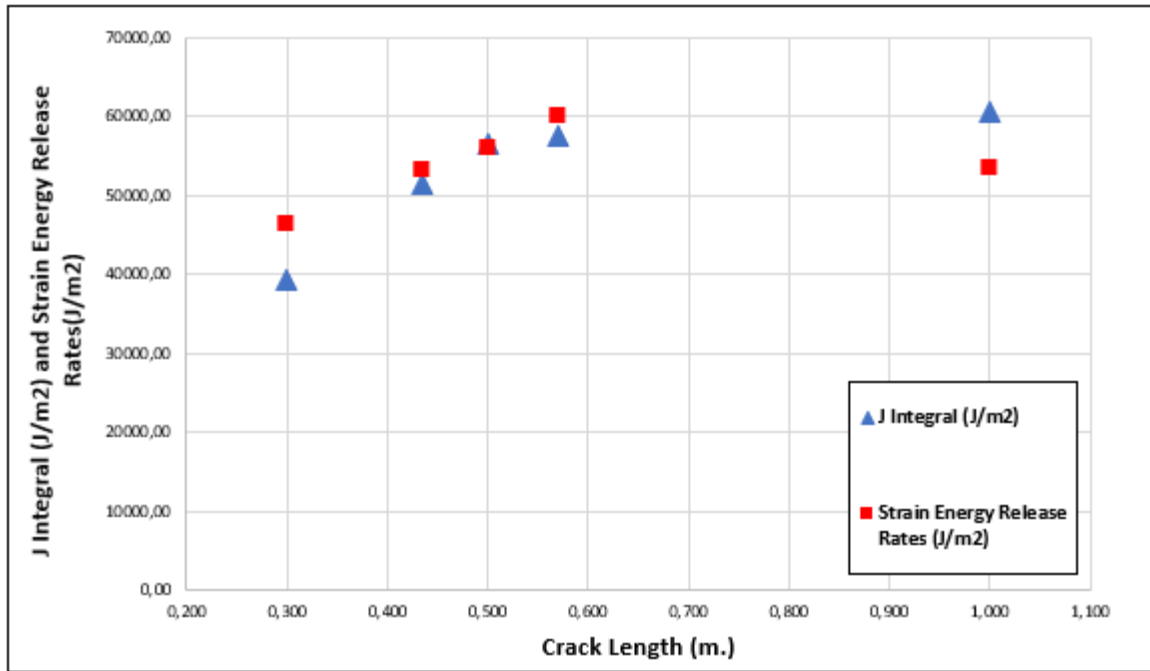


Figure 3.4. Crack length vs J Integral and strain energy release rate values (conventional method).

As the loading and boundary conditions are symmetric, stress distribution over the body is symmetric for both XFEM and FEM models. Von Mises stresses, stress concentration around the crack tip and crack opening sequence are shown in Figure 3.5 and Figure 3.6. In the FE model, Von Mises stress values changes depending on the stationary crack lengths. For both of the models, the highest stress value is obtained at the crack tip as expected.

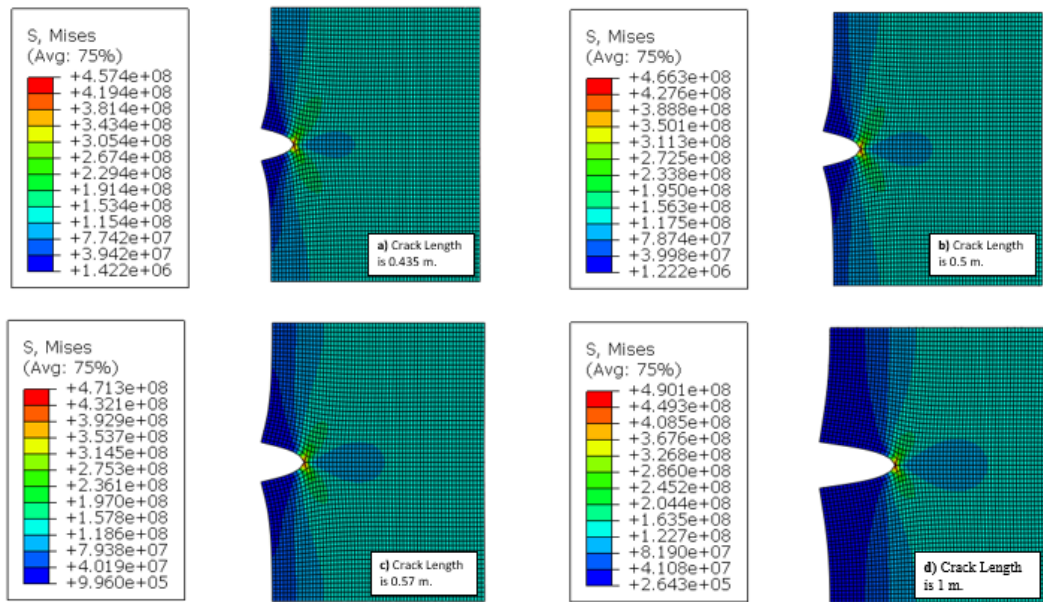


Figure 3.5. Crack openings for several stationary crack lengths (conventional method) for 1 mm displacement loading magnitude.

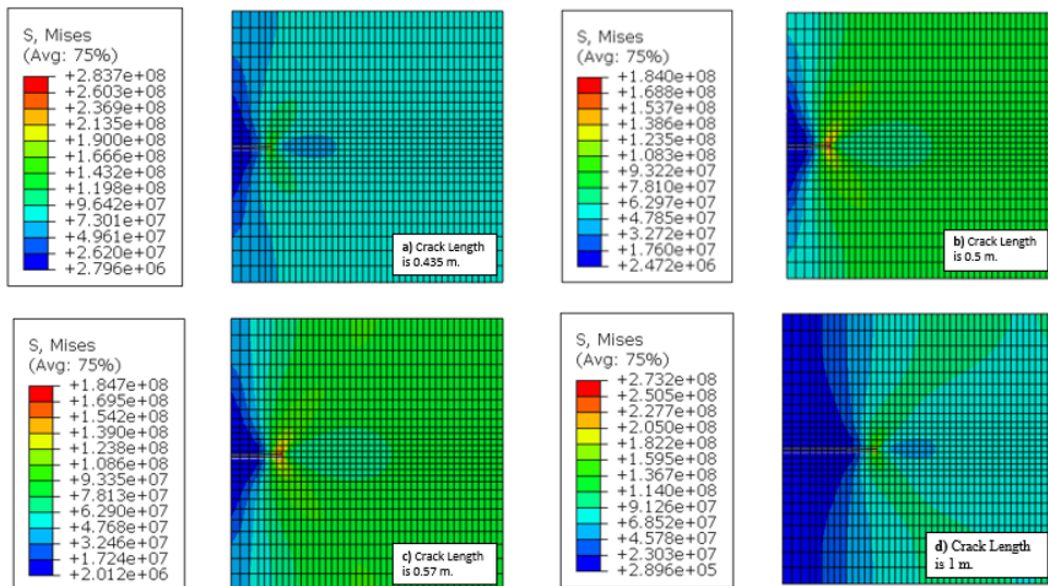


Figure 3.6. Crack openings for propagating crack (XFEM).

The energy stored in the body after loading is defined as strain energy. Some of the strain energy stored in the body contributes to the crack propagation if the damage initiation and propagation requirements are met. Therefore, strain energy values (ALLSE) must be decreasing with increasing crack size. Strain energy values calculated by XFEM and conventional FEM for several cracks are plotted and compared with each other. The main purpose of this comparison is to investigate if the strain energy values decrease with increasing crack length for both FEM and XFEM models. As it can be seen in Figure 3.7, strain energy values obtained by the XFEM are close to the strain energy values determined by the conventional FEM and their values decrease with crack propagation.

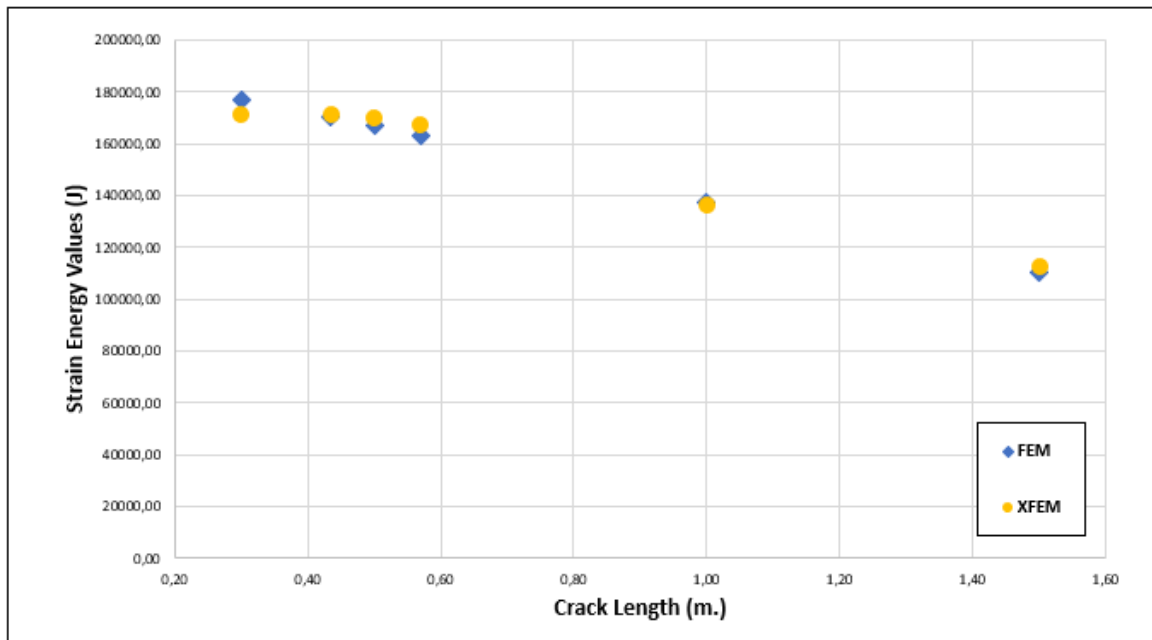


Figure 3.7. Crack length vs strain energy values for plane-strain models.

3.4. Three Dimensional Model

In this section, three dimensional model of a single edge notch specimen is completed. Both XFEM model for a propagating crack and FEM model for a stationary crack are used. Maximum stress values obtain by two dimensional and three dimensional FE models for 0.5 m stationary crack are compared. Additionally, maximum stress values determined by three dimensional FEM and XFEM models for 0.5 m crack are compared as well. The main purpose of the three dimensional model is to compare the reduction in strain energy values determined by XFEM and FEM models for 0.5 m and 0.57 m cracks.

3.4.1. Conventional Finite Element Method

3D modeling of the 0.5 m stationary crack is accomplished. In this model, conventional finite element method is used. 8 node linear brick element type (C3D8) is used. Total number of 78351 and total number of 72000 elements are used to complete the analysis. Von Mises stresses and stress concentrations around the crack front are shown in Figure 3.8.

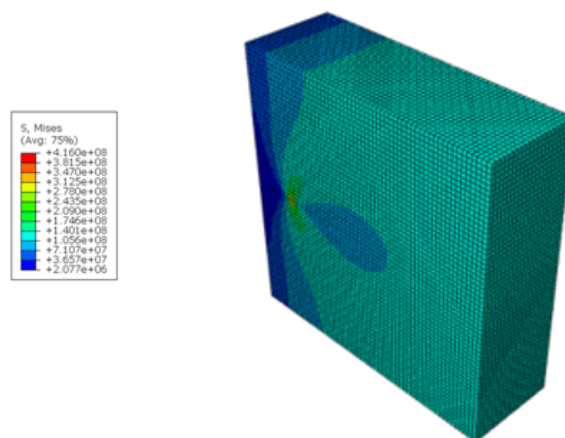


Figure 3.8. Conventional method (crack length is 0.5 m).

The value of the maximum Von Mises stress obtained at the crack front for three dimensional FEM model is in the range of 381-416 MPa, whereas the value of the maximum Von Mises stress obtained at the crack tip of the 0.5 m stationary crack for the two dimensional FEM model is equal to 427-466 MPa. By comparing these two stress values and stress fields shown in Figure 3.5 and Figure 3.8, it is observed that there is a non-negligible difference between the maximum Von Mises stresses and stress fields around the crack tip and crack front for the two dimensional and three dimensional models respectively for 0.5 m stationary crack. For the single edge notch specimen subjected to uniaxial tension, far from the notch tip, the plate is in the plane stress state. However, actual stress and strain components at the notch tip are 3D. This results in higher Von Mises stress values comparing to the three dimensional case, which take into account all three principal stress components. Therefore, it is expected that the value of the Von Mises stress at the notch tip determined in the two dimensional model is higher than the value of the Von Mises stress at the crack front determined in the three dimensional model [19].

3.4.2. Extended Finite Element Method (XFEM)

In this section, three dimensional modeling for the propagating crack is modeled. In this model, extended finite element method is used. Crack propagates according to the selected damage criterion and parameters. Number of nodes and elements are 6337 and 5160. C3D8 (8 node linear brick element with full integration) type element is used. Von Mises stresses and stress concentrations around the crack tip are shown in Figure 3.9.

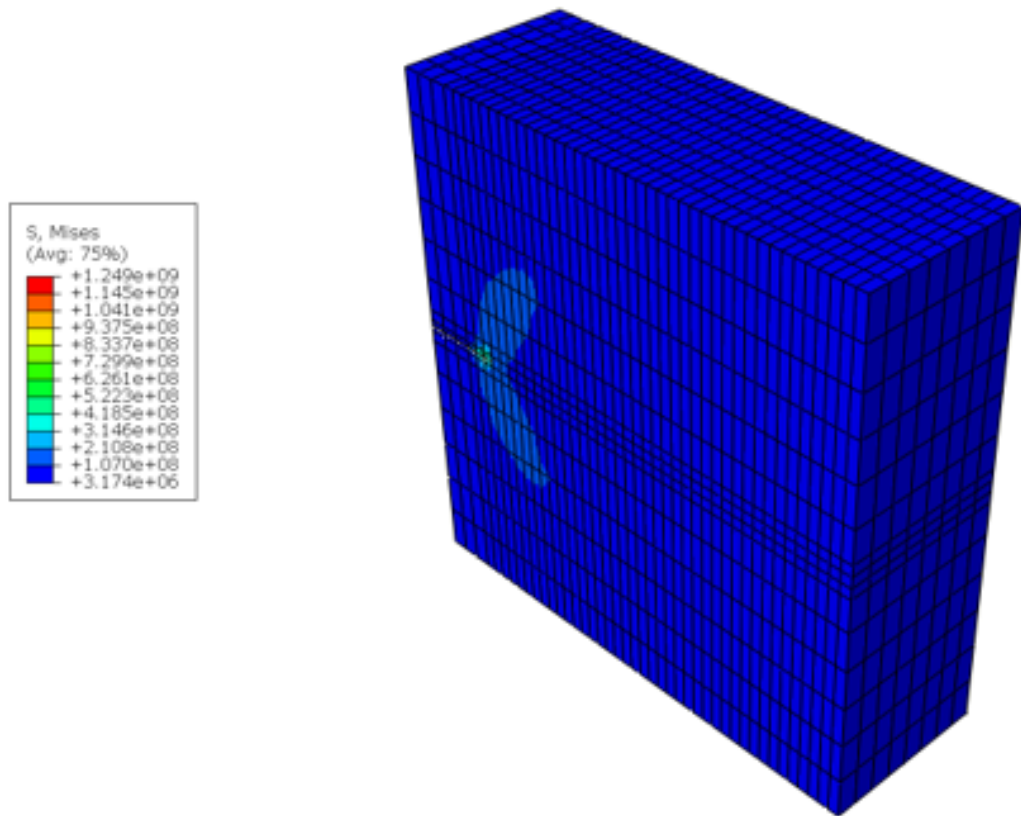


Figure 3.9. XFEM 3D (crack length is 0.5 m).

The value of the Von Mises stress obtained at the crack front for three dimensional XFEM model is in the range of 314-419 MPa, whereas it is in the range of 427-466 MPa for 3D FEM model. Finer mesh is required in order to compare stress values for both methods accurately. However, significant difference in two maximum stress values is observed. The reason of this difference is that in XFEM, stress concentration is firstly at the crack notch, 0.3 m crack. After the damage initiation, when the crack starts to propagate stress concentration is always at the crack front, nevertheless, in conventional FEM, stress concentration is always at the notch tip (0.5 m) and stress values increase as long as loading is applied. In other words, modeling propagating and stationary cracks causes difference in stress values and stress distributions determined by XFEM and FEM.

3.4.3. Results

The values of the strain energy (ALLSE) for both models are compared and plotted in Figure 3.10 and Table 3.4. As the XFEM crack propagates, time is noted when the crack is at 0.5 m length. According to Figure 3.10, crack starts to propagate at time $t=0.660279$ seconds and at time $t=0.700902$ seconds is at length 0.5 m in the XFEM model. At this time, strain energy value decreases drastically as crack propagates to 3 m in a very short time period. For the stationary crack, that is a non propagating crack, strain energy value keeps increasing until the end of the time step.

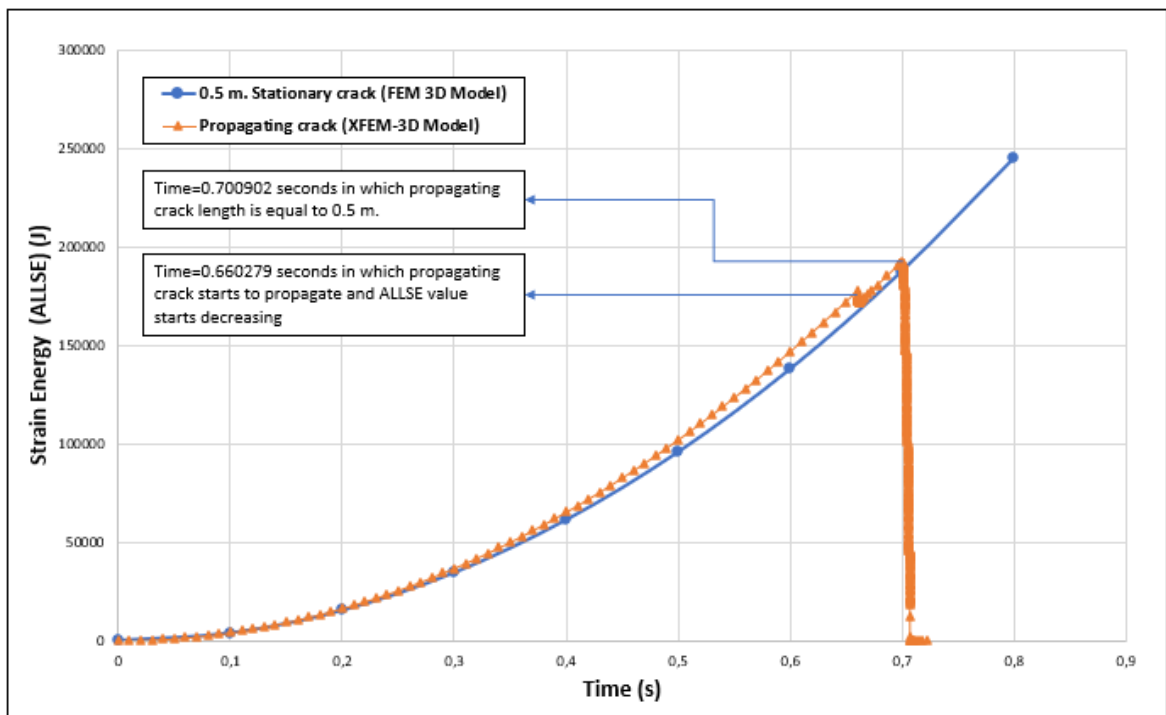


Figure 3.10. Strain energy comparison between XFEM and conventional method for 0.5 m crack.

Table 3.4 shows the strain energy values for 0.5 m and 0.57 m cracks for the XFEM and conventional methods for both plain-strain (2D) and 3D models. For the two dimensional models, difference between strain energy values obtained from FEM and XFEM are 1.8% and 2.7%, respectively. For the three dimensional models, difference

between strain energy values obtained from FEM and XFEM are 1.9% and 1.3%, respectively. According to the percentage differences, strain energy values obtained from XFEM and conventional contour integral methods for 0.5 m and 0.57 m cracks are very close. However, there is a significant change in the strain energy values between two dimensional and three dimensional cases. This difference is possibly originated from the plane strain assumption made in the two dimensional model.

Table 3.4. Strain energy value (ALLSE) (J) comparison between 3D and plane strain (2D) models of both XFEM and conventional FE methods for 0.5 m and 0.57 m cracks respectively(%: percentage difference, ΔU : strain energy difference between XFEM and FEM).

2D				3D			
FEM	XFEM	ΔU	% D	FEM	XFEM	ΔU	% D
167066	170013	2947	1.8	188024	191596	3572	1.9
163135	167577	4442	2.7	183633	186051	2418	1.3

For crack propagation analysis, one of the most important quantities to be considered is the change in the strain energy value between two cracks. The difference between the change in the strain energy values (from 0.5 m to 0.57 m crack) for two dimensional FEM and XFEM models is 46.96%. The difference between the change in the strain energy values (from 0.5 m to 0.57 m crack) for three dimensional FEM and XFEM models is 23.23%. There is a significant difference between the change in the strain energy values for FEM and XFEM.

3.4.4. Correlation Trial between Energy Dissipated in Whole Model (XFEM) and J Integral (FEM)

In the XFEM analysis, J integral cannot be requested for a propagating crack. Therefore, a variable that would allow calculation of energy release rate is investigated. ALDMD, the energy dissipated in the whole model, seemed a possible candidate for

this purpose. ALLDMD values can be requested for each time step or displacement applied on the geometry as it can be seen in Figure 3.11. In this section, the goal is to investigate the relationship between J integral value and ALLDMD.

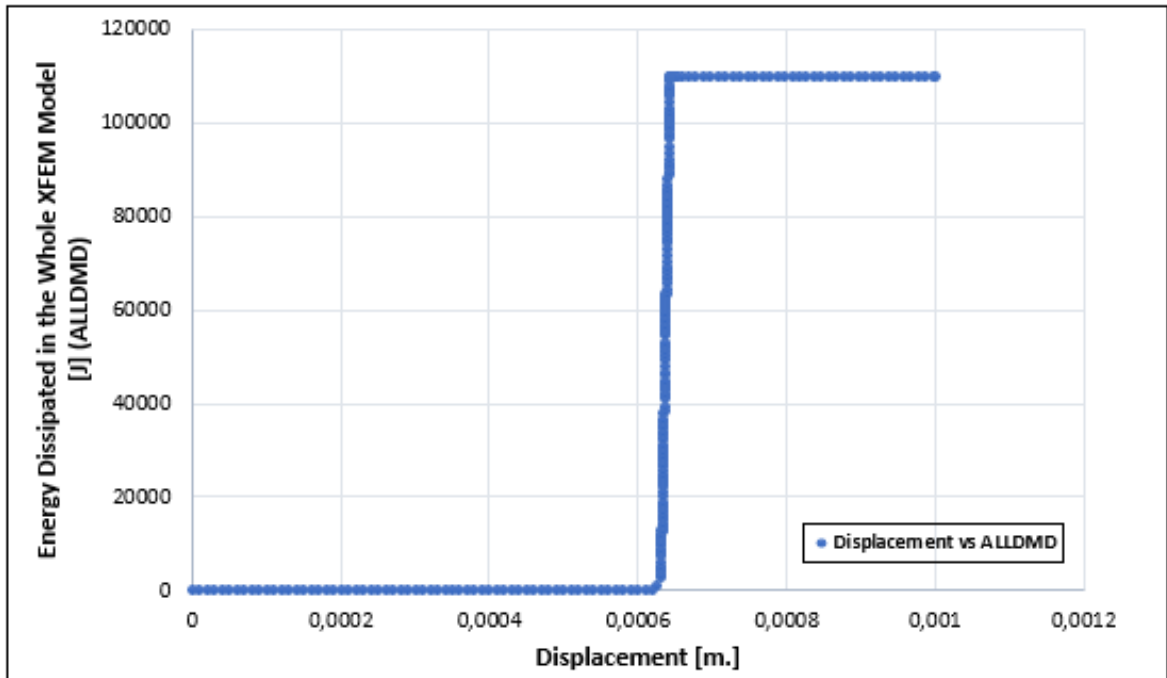


Figure 3.11. Displacement applied on the geometry vs ALLDMD value for XFEM model.

For stationary crack analysis, recoverable strain energy stored in the body (ALLSE) and total strain energy (ALLIE) have the same value as crack does not propagate, consequently, the value of the energy dissipated by damage (ALLDMD) is zero. However, for the propagating crack analysis, strain energy stored in the body and total strain energy values are not equal as energy is dissipated by damage.

Figure 3.12 and Table 3.5 show the comparison of energy dissipation predicted from XFEM and energy released between two crack lengths as predicted from FEM. Change in the crack length (Δa) is calculated by the difference of the crack lengths from 0.3 m crack length. Change in the J integral values (ΔJ) for two different cracks are determined by calculating the change in the J integral values between 0.3 m crack

and following crack. The later ($\Delta a * \Delta J$) is calculated by multiplying the J integral difference value by the change in crack length. For small crack increments, ALLDMD values are very close to those obtained from the J integral values. However, for large change in the crack length, the difference becomes very large.

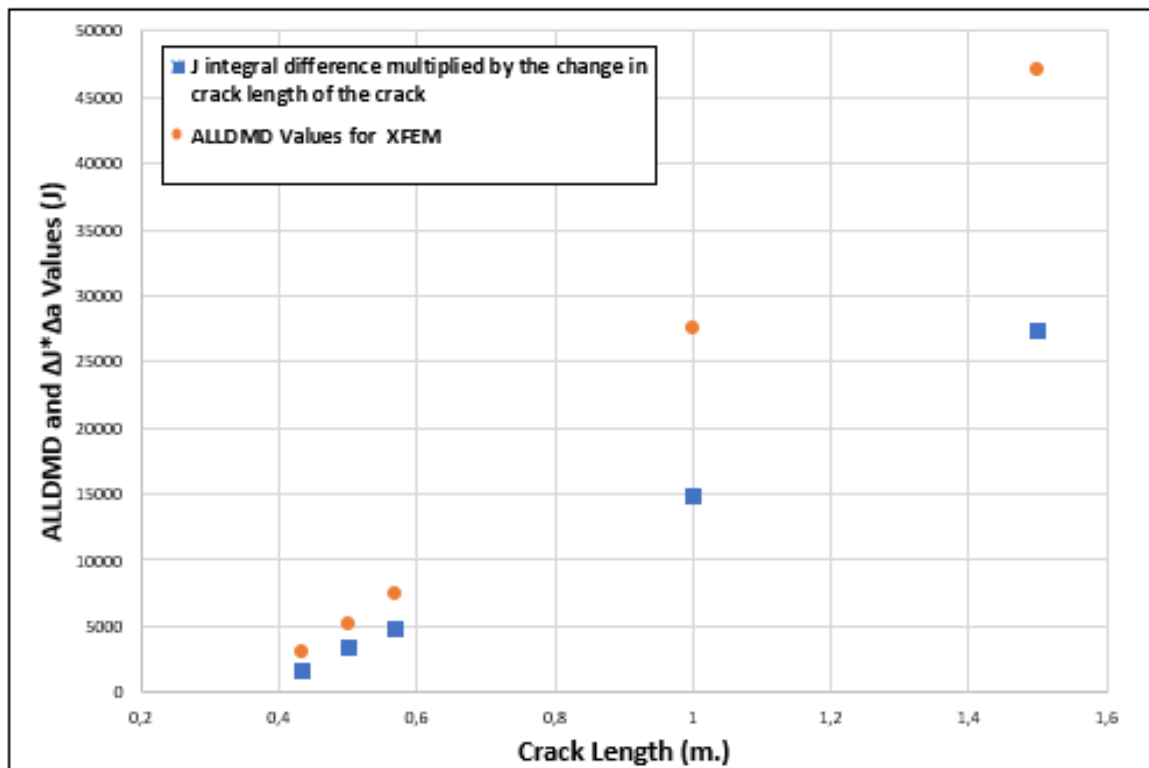


Figure 3.12. J Integral difference multiplied by propagated crack length (conventional method) vs ALLDMD values obtained with XFEM model.

Table 3.5. Comparison between the J Integral values and strain energy release rates determined by the conventional method (\mathbf{a} : crack length, \mathbf{U} : strain energy, ALLDMD: dissipated strain energy).

\mathbf{a} (\mathbf{m})	$\Delta\mathbf{a}$ (\mathbf{m})	J Integral (\mathbf{J}/\mathbf{m}^2)	$\Delta\mathbf{J}$ (\mathbf{J})	$\Delta\mathbf{a} * \Delta\mathbf{J}$ (\mathbf{J})	ALLDMD (\mathbf{J})
0.3	-	39458	-	-	-
0.435	0.135	51568	12109	1634	1414
0.5	0.20	56681	17222	3444	4725
0.57	0.27	57456	17697	4778	6117
1	0.70	60672	21214	14849	26101
1.5	1.2	62237	22778	27778	45634

3.4.5. Conclusions of the Benchmark Problem

Main conclusions of the benchmark study are:

- J integral values are in good agreement with the energy release rate calculated as the change in strain energy per change in crack length.
- J integral cannot be requested as a history output in XFEM for a propagating crack.
- In XFEM, crack does not need to be located on the element face or edges. Therefore, in conventional method, re-meshing is required. For this reason, XFEM is preferable for being cost effective method where it is applicable.
- Strain energy values (ALLSE) obtained by the conventional FE method and XFEM method are close to each other in 2D and 3D models.
- Strain energy values calculated for 0.5 m and 0.57 m cracks for two dimensional FEM and XFEM models are within 2.7%.
- Strain energy values calculated for 0.5 m and 0.57 m cracks for three dimensional FEM and XFEM models are within 1.9%.

- The decrease in the values of the strain energies between two cracks (0.5 m and 0.57 m crack) for 2D FEM and XFEM models quite close to each other.
- The decrease in the values of the strain energies from 0.5 m crack to 0.57 m crack for two and three dimensional FEM and XFEM models are not significantly close.
- There is a significant difference between the strain energy values obtained from two dimensional and three dimensional models for both FEM and XFEM.
- For small crack advances, dissipated energy values obtained from the XFEM are very close to those based on J integral values calculated from FEM. If crack growth is large, difference between two values becomes much more severe.
- For future developments and justifications related to ALLDMD parameter, propagating interface crack model can be investigated by XFEM and the ALLDMD results can be compared with the conventional FE analysis for several cracks having very small increments.

4. 2D CRACK MODELING IN A BEARING UNDER COMPRESSION

In this chapter, two dimensional axisymmetric finite element model of a circular elastomeric isolation bearing is presented. Due to symmetry, half of the single rubber pad is used and both bonded and unbonded conditions are studied. Filled natural rubber is used for the rubber material. Only compression loading is applied on the body. The effects of fillet radius at sharp corners and coefficient of friction on the convergence of the finite element analysis are investigated. Afterwards, stationary interface cracks are modeled and J integral values are calculated. The tearing energy and stiffness degradation for various crack lengths are compared with the data obtained from the literature.

4.1. Axisymmetric Model of the Elastomeric Bearing

In this thesis, elastomeric isolation bearing with circular cross-section and consisting of two rubber pads and one metal shim sandwiched between the rubber pads is investigated. The bearing is shown in Figure 4.1.

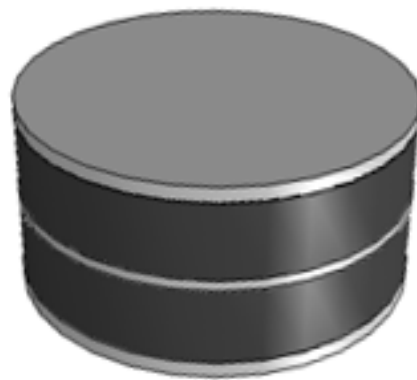


Figure 4.1. Circular elastomeric isolation bearing.

As the geometry, loading, material properties and boundary condition of the elastomeric bearing are symmetric, axisymmetric model is used. Several stationary cracks are located at the interface between the rubber pad and metal plate/shim such that it is sufficient to model half of the rubber pad with a single crack. The geometry, dimensions, axis of symmetry, rubber pads, metal shims and axisymmetric model in consideration are shown Figure 4.2.

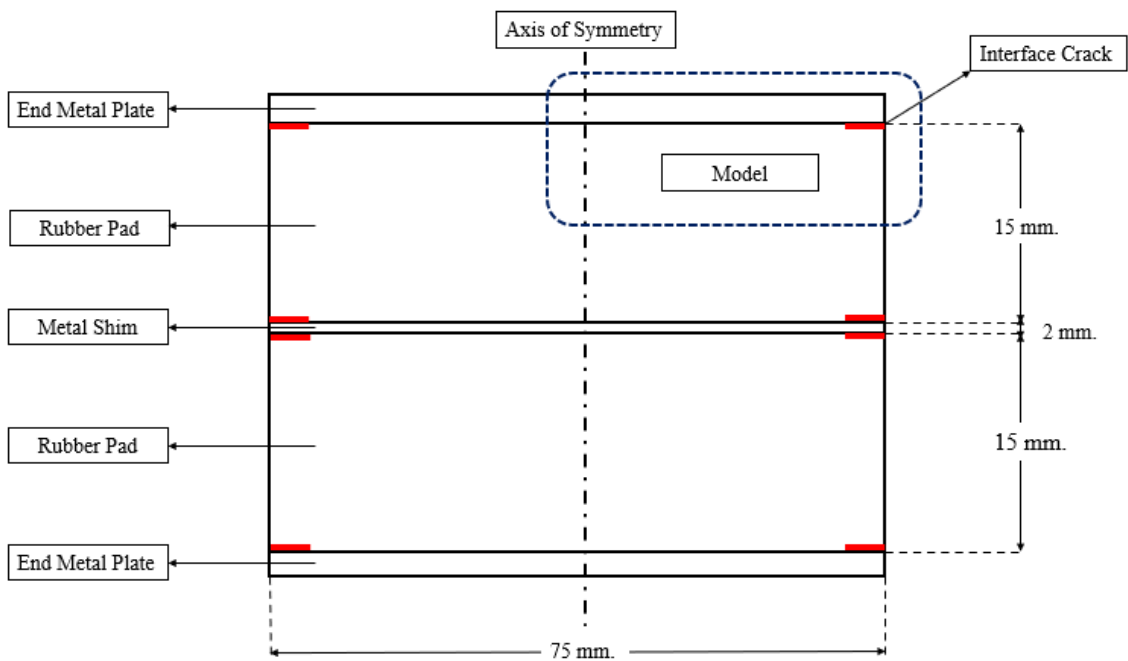


Figure 4.2. Geometry of the elastomeric rubber bearing.

4.2. Finite Element Model

In this section, model parameters used to investigate the interface crack problem such as material parameters, loading, boundary conditions and mesh structure are explained.

4.2.1. Material Model

The rubber pad is assumed to be filled natural rubber. As it is explained in the Section 2.1.2, Yeoh hyper-elastic elastic model performs well in terms of computational efficiency, accuracy and test data needed for calibration of the model. The Yeoh parameters used in the study are tabulated in Table 4.1.

Table 4.1. Yeoh-parameters for natural rubber.

K (Pa)	D_1 (1/Pa)	C_{10} (Pa)	C_{20} (Pa)	C_{30} (Pa)
2100E+6	9.524E-10	486900	39200	1170

4.2.2. Geometry of the Axisymmetric Model

Geometry of the half rubber pad is shown in Figure 4.3.

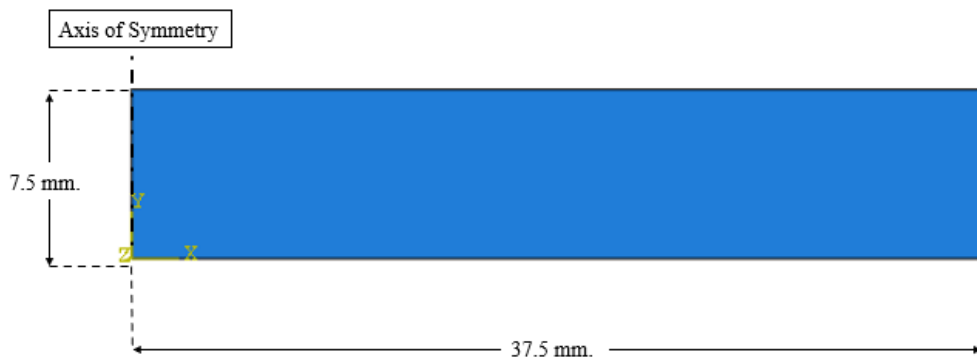


Figure 4.3. Geometry of the half rubber pad.

The end metal plates are modeled as analytical rigid surfaces. This representation does not require any mesh, consequently it is cost effective. Analytical rigid plate with straight edges and analytical rigid plates with an edge fillet with different fillet radius values are used in the analysis. The geometries of the analytical rigid plates are shown in Figure 4.4.

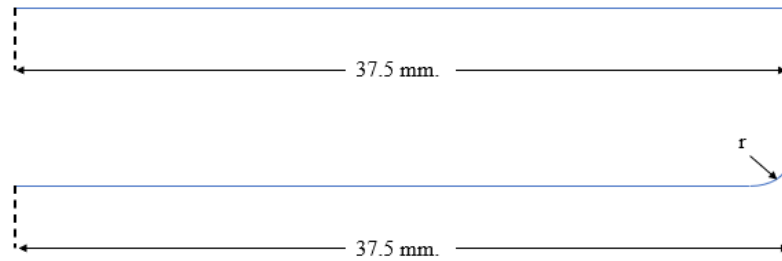


Figure 4.4. Geometry of the analytical rigid plate.

4.2.3. Mesh of the Axisymmetric Model

Mesh is composed of 12375 8 node-biquadratic axisymmetric quadrilateral, hybrid, linear pressure (CAX8H) elements and 37942 nodes. As interface crack is located between the analytical rigid plate and the top surface of the rubber, finer mesh is required near the top surface of the rubber. Location of the initial crack, dimensions of the geometry and the mesh are shown in Figure 4.5.

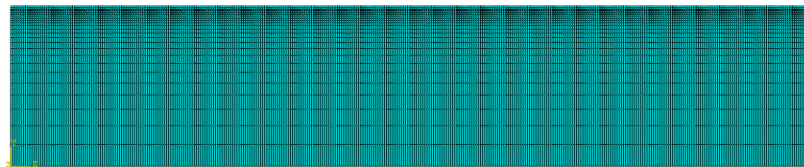


Figure 4.5. Mesh of the axisymmetric model.

4.2.4. Boundary Conditions and Loading

Boundary conditions, loading and location of the interface crack are shown in Figure 4.6.

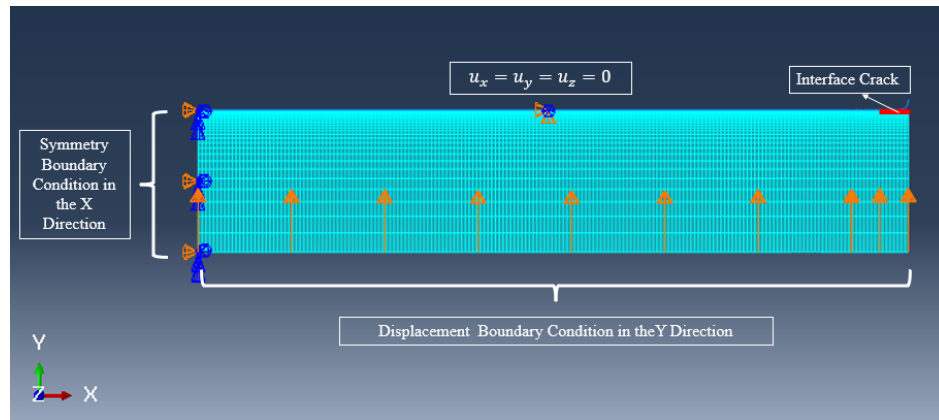


Figure 4.6. Boundary conditions, loading of the axisymmetric model and location of the interface crack.

Displacements corresponding to 10, 20, 25, 30 and 35% compression strains are applied on the bottom surface of the half rubber pad. Symmetry boundary conditions are applied on the left surface. Analytical rigid body is placed on the top surface of the rubber to represent a steel plate. Three different methods of fixing the top surface of the rubber to the analytical rigid plate are investigated and their effects on the convergence time is studied. One method is to tie the top surface of the rubber not containing crack to the analytical rigid plate and to pin the reference point on the analytical rigid plate. The second method is to place analytical rigid plate only on the top of the crack surface and to tie the top surface of the rubber not containing crack to the reference point on the analytical rigid plate. The third method is to constrain top surface of the rubber not containing crack in every direction and to place analytical rigid plate on the crack surface.

4.2.5. Contact Interactions

Contact interaction between the analytical rigid plate surface and top surface of the rubber is defined. Normal and tangential contact properties used in the analysis are shown in Table 4.2. Penalty method is used for friction formulation. The effect of coefficient of friction values on the convergence of the problem is investigated.

Table 4.2. Interaction properties between analytical rigid plate and crack surface.

Normal Behaviour	Tangential Behaviour (Friction Formulation: Penalty) Coefficient of Friction
Hard Contact	0.30
	0.25
	0.225
	0.215
	0.205
	0.20

4.2.6. Geometrical Improvements of the Analytical Rigid Plate

Crack analysis of a rubber material subjected to compression loading including interface crack is a difficult numerical problem. The elements near the edge of the analytical rigid plate get distorted significantly when analytical rigid plate with straight edge is used. These element distortions cause convergence problems, hence, at large compression loads result in convergence to stop. Therefore, the effects of smoothing the edges of the analytical rigid plate by introducing fillets on the convergence is investigated. Four different fillets having 0.5, 0.25, 0.20, 0.10 mm radius are used. The results are compared with the no fillet case.

4.3. Results and Discussion

Initially, finite element analysis of a bonded and unbonded elastomeric isolation bearing subjected to 35% compression is performed. The bonded case is modeled by applying tie constraint between the analytical rigid plate's surface and the top surface of the rubber. Converged solution up to 6.03% is obtained. Deformed shape and distorted elements are shown in Figure 4.7.

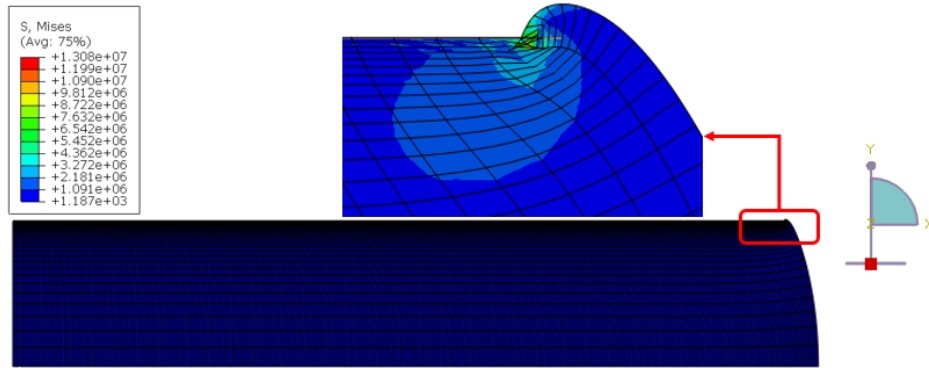


Figure 4.7. The deformed shape of the rubber subjected to 35% compression strain for bonded elastomeric isolation bearing (achieved compression strain=6.03%).

To model the unbonded case, contact property is defined between top surface of the rubber and analytical rigid plate. For frictionless tangential behaviour, convergence is achieved only up to 3.15% compression. Tangential behavior is defined as frictionless as well as with friction. Various coefficients of friction and the corresponding maximum strain for which convergence is achieved are given in Table 4.3. Figure 4.8 shows the deformed shape and element distortions near the edge of the analytical rigid plate of the unbonded elastomeric isolation bearing with coefficient of friction value of 0.25, the value for which the highest converged compression amount is reached.

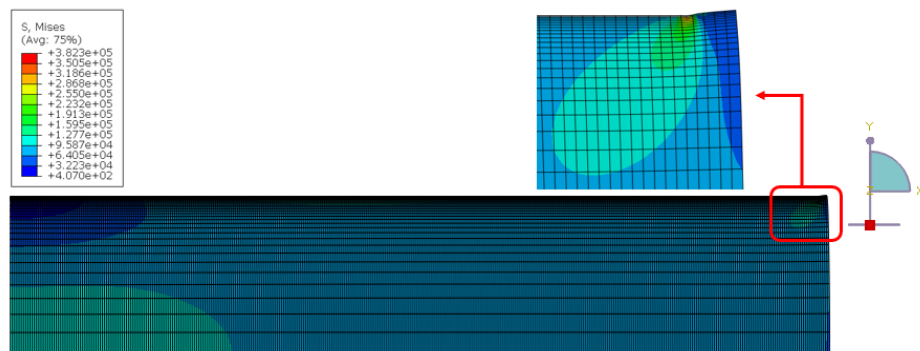


Figure 4.8. The deformed shape of the rubber subjected to 35% compression strain for unbonded elastomeric bearing (achieved compression strain=3.33%).

Table 4.3. Coefficient of friction values between analytical rigid plate and top surface of the rubber for the unbonded bearing not containing crack and fillet versus compression obtained.

Coefficient of Friction Value	Compression Obtained (%)
Frictionless	3.15
0.20	1.06
0.25	3.33
0.50	1.41

4.3.1. The Effect of Fillet Radius on the Convergence of the Unbonded Bearing

Due to limited convergence of the model with analytical plate with sharp corner, an alternative model with a fillet placed on the edge of the analytical rigid plate is constructed. The effect of friction coefficients on the convergence behaviour of the alternative model is also investigated.

Table 4.4. Coefficient of friction value between analytical rigid plate and top surface of the rubber for the model not containing any crack versus compression obtained.

Coefficient of Friction Value	Compression Obtained (%) with 0.5 mm fillet	Compression Obtained (%) without fillet
Frictionless	21.20	3.15
0.20	16.40	1.06
0.25	35	3.325
0.50	35	1.41

Table 4.4 shows the fillet radii and coefficient of friction values that were used, as well as the corresponding maximum compression values for which convergence was achieved. 35% compression is obtained for 0.5 mm fillet radii with coefficient of friction values of 0.25 or 0.50. For unbonded elastomeric bearing not containing crack, the

deformed shape of the rubber for 0.25 coefficient of friction, 0.5 mm fillet radius is shown in Figure 4.9.

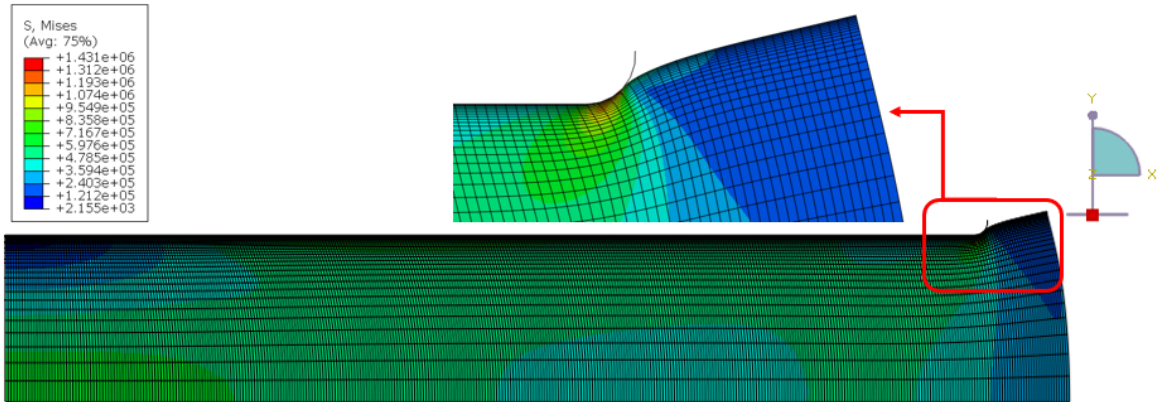


Figure 4.9. The deformed shape of the rubber subjected to 35% compression strain for unbonded elastomeric isolation bearing not containing interface crack for 0.25 coefficient of friction, 0.5 mm fillet radius (achieved compression strain=35%).

4.3.2. The Effects of Fillet Radius on the Convergence of the Bonded Bearing

In this section, finite element analysis for a bonded bearing with an edge fillet is performed. The effects of fillet radius on the solution convergence is studied for the selected bearing type. 0.5 mm fillet radius is used for this analysis. To simulate the bonded bearing, top surface of the rubber is tied to the analytical rigid plate's surface except a very small portion of the top surface of the rubber remaining under the fillet. On this small portion, contact property is defined between the analytical rigid plate and top surface of the rubber such that hard contact is selected for the normal behaviour and coefficient of friction value is set to be 0.25 for the tangential behaviour and penalty method is used for this behaviour. The convergence is obtained up to 22.02% compression strain. The deformed shape of the rubber and the distorted elements near the edge are shown in Figure 4.10.

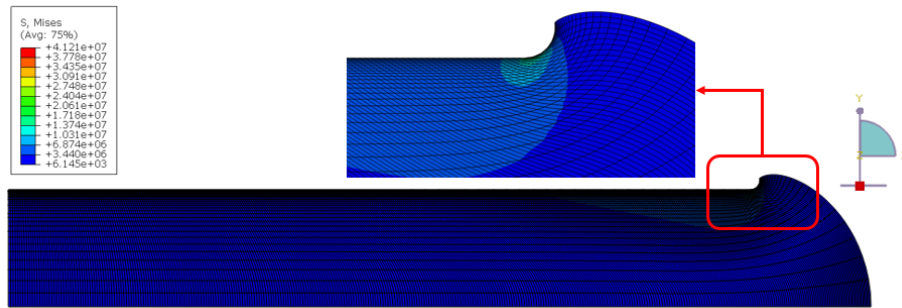


Figure 4.10. The deformed shape of the rubber subjected to 35% compression loading for bonded elastomeric bearing (22.02% compression strain is achieved).

The reaction forces versus displacement values obtained from the analysis are compared to those obtained in a previous simulation in Table 4.5. The agreement of the results is considered sufficient evidence for the verification of the bonded model described above.

Table 4.5. Reaction force for bonded elastomeric bearing without crack.

Compression Applied (%)	Vertical Reaction Force obtained from the model (kN)	Vertical Reaction Force obtained from the literature(kN)
10	6.2	7.0
15	10.7	11.0
20	17.0	17.0

4.3.3. Interface Crack Analysis for Bonded Bearing

In this section, stationary cracks of various lengths are placed at the interface between the analytical rigid plate and the top surface of the rubber. Contact property is defined between the crack surface of the rubber and analytical rigid plate. Hard contact is selected for the normal behaviour and coefficient of friction value is set to be 0.25 for the tangential behaviour and penalty method is used. The rest of the

rubber surface is tied to the analytical rigid plate's surface and is fixed in all directions. Analytical rigid plate is modeled with 0.5 mm fillet radius at the edge. 35% compression strain is applied to the bottom surface of the rubber. Deformed shapes for the 2.5 mm and 15 mm interface cracks are illustrated in Figure 4.11 and Figure 4.12.



Figure 4.11. The deformed shape of the bonded bearing subjected to 35% compression strain with 2.5 mm interface crack (achieved compression strain=35%).

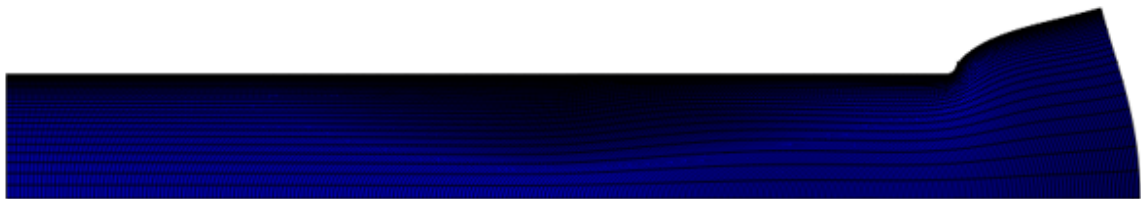


Figure 4.12. The deformed shape of the bonded bearing subjected to 35% compression strain with 15 mm interface crack (achieved compression strain=35%).

Due to the existence of interface cracks, elements near the edge of the rubber are not adhered to the analytical rigid surface. Consequently, convergence for 35% compression strain is accomplished. Various coefficients of friction studied and the corresponding reaction forces and compression strains are tabulated in Table 4.6. As it can be seen in Table 4.6, the predicted reaction force value is closest to the reaction force value from the literature. This value is for 0.205 coefficient of friction. This value is used in the analysis that follows.

The effect of fillet radius on the response of the bonded bearing subjected to 35% compression strain and containing 15 mm interface crack is summarized in Table 4.7.

Table 4.6. Reaction forces and compression strains obtained for different values of coefficient of friction for the bonded bearing with a 15 mm interface crack.

Coefficient friction	Reaction force determined from ABAQUS (kN)	Reaction force obtained from literature (kN)	Compression obtained (%)
0.10	-	-	7.87
0.20	-	-	7.12
0.205	18.70	17.10	35
0.215	19.04	17.10	35
0.225	19.41	17.10	35
0.25	20.50	17.10	35
0.30	23.30	17.10	35

Table 4.7. Reaction forces and compression strains obtained for different values of fillet radii for the bonded bearing with a 15 mm interface crack.

Fillet radius (mm)	Reaction force determined from ABAQUS (kN)	Reaction force obtained from literature (kN)	Compression obtained (%)
0.50	18.70	17.10	35
0.25	18.83	17.10	35
0.20	13.85	17.10	30.63
0.10	8.01	17.10	22.61
0	1.03	17.10	3.98

As it is seen in Table 4.7, the predicted reaction force is closest to that in the literature for the fillet radius of 0.50 mm. When the value of the fillet radius is below

0.25, full convergence of the solution is not achieved. However, there is no significant difference in the reaction force values determined from the model with 0.5 mm and 0.25 mm fillet radii.

4.3.4. Run Time (Convergence Time) Improvement

As three dimensional interface crack model will be considered in the following chapter, it is important to reduce the run time while maintaining accuracy. Thus, three different models are constructed to improve the run time of the finite element analysis of axisymmetric model with a 15 mm interface crack. For this analysis, 2.5 mm fillet radius is used for the analytical rigid plate and coefficient of friction value is set to 0.205. First model is to model analytical rigid plate on the whole top surface of the rubber. Top surface of the rubber not containing crack is tied to the analytical rigid plate's surface and rigid plate is fixed with a reference point. Second model is to model analytical rigid plate only on the crack surface of the rubber and zero displacement boundary condition is assigned on the the top surface of the rubber not containing crack. Third model is to model analytical rigid plate only on the crack surface of the rubber and top surface of the rubber not containing crack is tied to a fixed reference point located on the analytical rigid plate. For all the models, same J integral value is obtained with different run times as it can be seen in Table 4.8.

Table 4.8. Run time and J integral values for all of the models.

Model number	Run time (sec.)	J integral Value (J/m²)
Model 1	2525	7971
Model 2	2954	7971
Model 3	2323	7971

By modeling analytical rigid plate only on the crack surface of the rubber and by using tie constrain for fixing the rubber surface not containing crack to a reference point on the analytical rigid plate, run time, consequently cost of the finite element analysis

is reduced significantly. Therefore, for the following axisymmetric model analysis and three dimensional model, model 3 is preferred.

Coefficient of friction value is set to 0.205 and fillet radius value is set to 0.5 millimeter in order to compare reaction force results obtained from the model with the literature for 10, 20, 25, 30 and 35% compression strains. This analysis is performed for the initial 2.5 millimeter interface crack (non-propagating crack). The comparison of the reaction forces, J integral and tearing energy are shown in Table 4.9 and 4.10.

Table 4.9. Comparison of the reaction forces determined from the model with the reaction forces obtained from the literature.

Compression Strain %	Reaction force determined from ABAQUS (N)	Reaction force obtained from literature (N)
35	53.9	56.33
30	36.1	37.37
25	24.1	24.54
20	15.8	15.9
10	5.8	5.8

Table 4.10. Comparison of the J Integral values determined from the model with the tearing energy values obtained from the literature.

Compression Strain %	J Integral determined from ABAQUS (kJ/m²)	Tearing energy obtained from literature (kJ/m²)	Strain energy for the whole model (J)
35	16.8	9.84	44.8
30	10.0	6.06	28.2
25	5.9	3.78	17.0
20	3.3	1.73	9.6
10	0.73	-	2

It can be seen in Table 4.9 that the predicted reaction forces are close to the ones obtained from the literature. This is not the case for the J integral and tearing energy results as it is illustrated in Table 4.10. The reason of this deviation is that tearing energy values obtained from the literature is a polynomial fit. Therefore, tearing energy values for 2.5 mm non-propagating crack for 35, 30, 25, 20 and 10% compression strains are not the exact values rather they are approximate values.

The procedure applied for the 2.5 mm stationary crack is applied for 3, 5, 8 and 15 mm cracks. Comparison of the reaction forces as well as the stiffness reduction due to cracks can be seen in Figure 4.13.

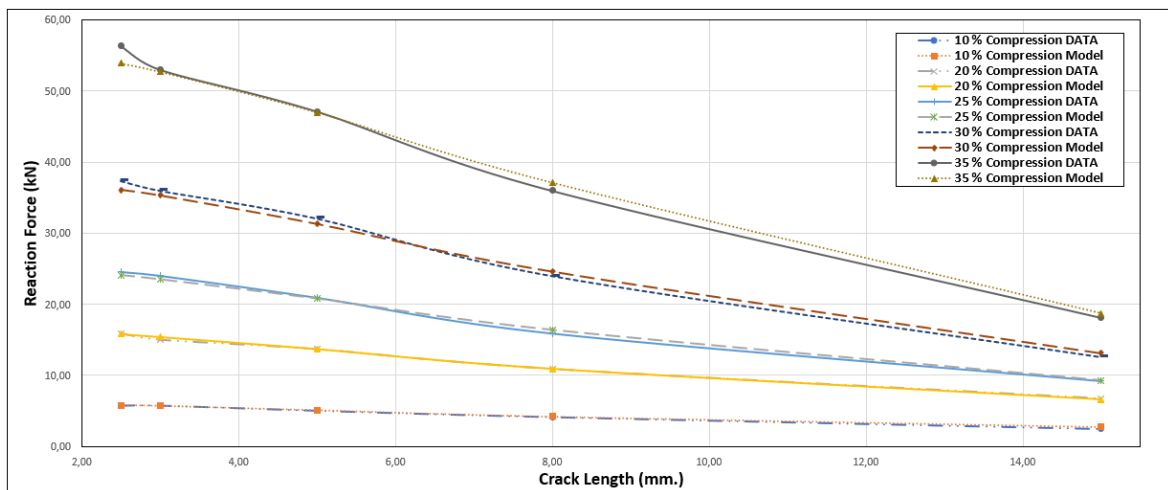


Figure 4.13. Reaction force values comparison for different values of compression strains and crack lengths.

It can be observed in Figure 4.13 that the predicted reaction force values are very close to the ones obtained from the literature for each compression strain and crack length.

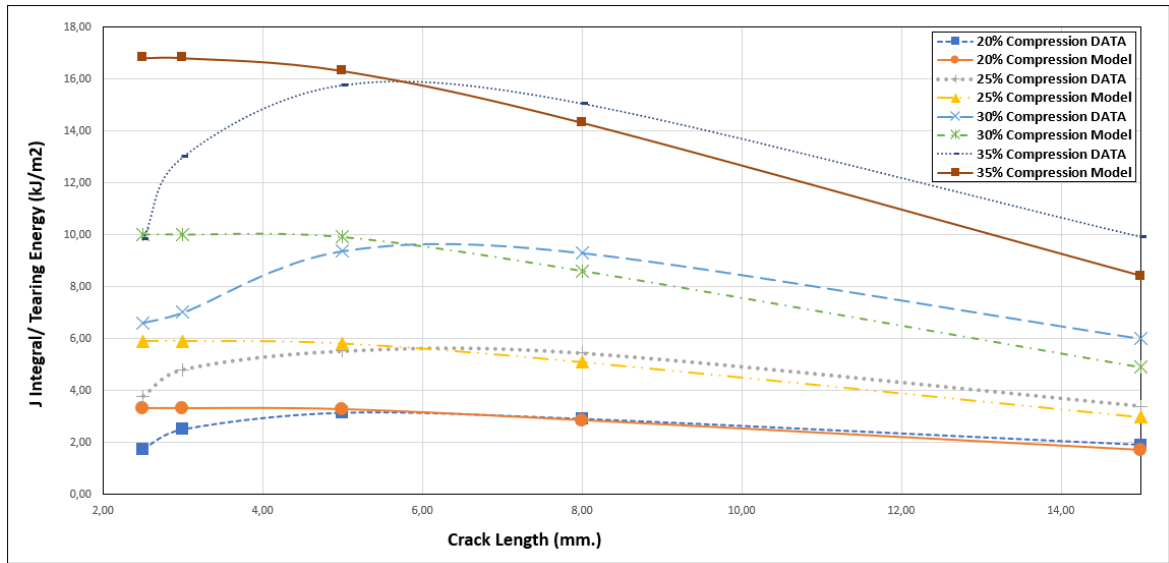


Figure 4.14. J integral and tearing energy comparison for different values of compression strains and crack lengths.

In Figure 4.14, J integral values calculated for each crack length and each compression strains applied on the rubber are compared with the results from the literature. For 5 mm and longer crack, the agreement is very good. For 2.5 and 3 mm, on the other hand, some deviation is present.

4.3.5. Conclusions of the Axisymmetric Model Problem

Main conclusions of the axisymmetric model study are:

- For the bonded and unbonded bearing models without a fillet, very small amount of compression is obtained (bonded case: 6.03%, unbonded case: 3.33%) to element distortions near the edge of the plate.
- For the unbonded bearing, for 0.25 and 0.50 friction coefficients and 0.50 mm fillet, convergence is obtained for 35% compression strain.
- For the bonded bearing with 0.5 mm fillet and for the coefficient of friction value of 0.25 the convergence is obtained up to 22.02% compression strain. The agreement of the results regarding the vertical reaction force values for several compression

strains with the literature is very good.

- Various coefficients of friction studied for the bonded bearing and concluded that the predicted reaction force value is closest to the reaction force value from the literature obtained for 0.205.
- For the bonded bearing containing 2.5 mm interface crack with 0.5 mm fillet and for the coefficient of friction value of 0.25 the convergence is obtained up to 35% compression strain. It is concluded that placing a interface crack at the edge of the plate overcomes the numerical difficulties of the solution. Same procedure is completed for 15 mm interface crack with the same model parameters. Full convergence for 35% compression strain is obtained as well.
- For the bonded bearing containing 15 mm interface crack, 0.25 mm or 0.50 mm fillet radii resulted in convergence for 35% compression strain, whereas for smaller or no fillets full convergence was not achieved.
- For the bonded bearing with 15 mm interface crack, 2.5 mm fillet radius and the coefficient of friction 0.205, by modeling analytical rigid plate only on the crack surface of the rubber, run time is significantly improved.
- For the bonded bearing with the coefficient of friction 0.205 and 0.5 mm fillet radius, reaction force results obtained from the bonded bearing model are agreed well with those from the literature for 10, 20, 25, 30 and 35% compression strains and for 2.5, 3, 5, 8 and 15 mm stationary cracks. J integral values determined for the bonded bearing model and tearing energy values obtained from the literature reasonably agree. The difference at small crack lengths may result from curve fit used in the literature data.

5. 3D CRACK MODELING IN A BEARING UNDER COMPRESSION AND SHEAR

In this chapter, three dimensional finite element model of a circular elastomeric isolation bearing subjected to compression and shear loading is constructed. Interface cracks of various lengths are modeled and J integral values for each interface crack are evaluated. The effects of fillet radius at sharp corners and coefficient of friction on the convergence of the finite element analysis are investigated.

5.1. Three Dimensional Model of the Elastomeric Bearing

In this section, material model, geometry of the rigid plate, loading and boundary conditions, mesh structure, contact properties between rigid plate and rubber and constraints applied on the rubber pad are explained. Two interface crack are modeled, separately, 2.5 mm and 15 mm.

5.1.1. Material Model

Filled natural rubber is selected for the rubber material. Yeoh hyper-elastic material model is used with the material parameters shown in Table 4.1.

5.1.2. Geometry

The geometry of the rubber pad and location of the interface cracks are shown in Figure 5.1. The end metal plate of the elastomeric isolation bearing is modeled as discrete rigid body. Crack is placed at the interface between the rubber pad and rigid plate. The geometry of the discrete rigid body is a partial cylinder. Rigid body has no material property, therefore, convergence time is expected to be reduced significantly. Furthermore, the study presented in the previous chapter showed that modeling analytical rigid plate only on the crack surface of the rubber and using tie constraint

between the top surface of the rubber not containing crack and a fixed reference point located on the analytical rigid plate decreases the run time. Therefore, in 3D model, discrete rigid plate is placed only on the crack surface. The geometries of the discrete rigid plates used in the 2.5 mm and 15 mm stationary cracks are shown in Figure 5.2.

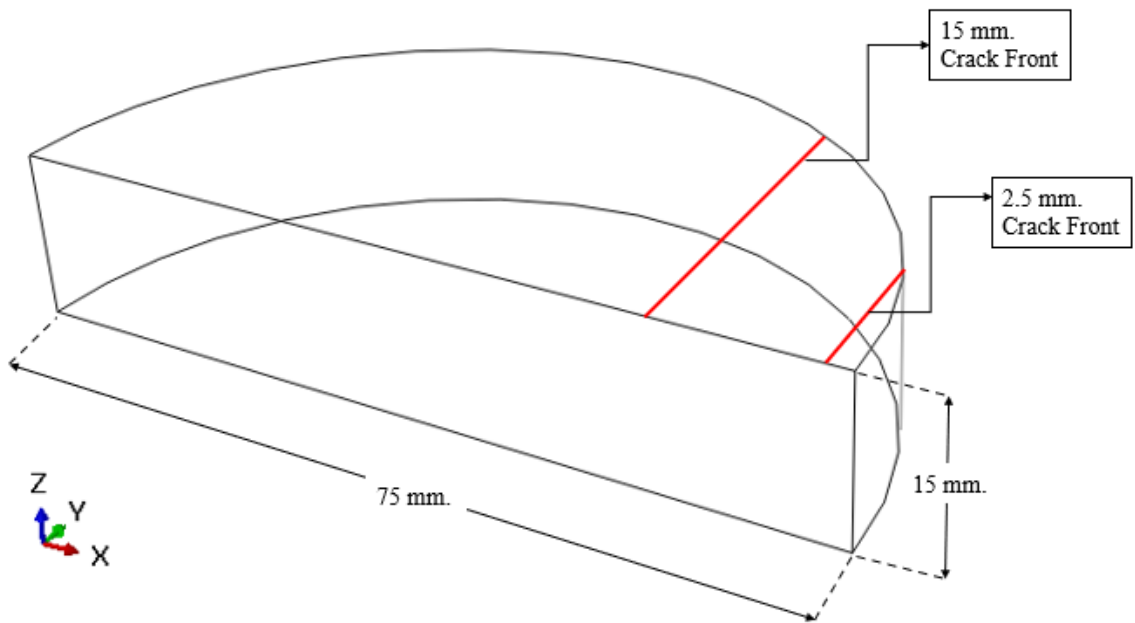


Figure 5.1. Geometry of the three dimensional elastomeric isolation bearing model.

In order to prevent element distortions near the edge of the discrete rigid plate, edge fillet with 0.05 mm and 0.1 mm radius is placed on the plate. Afterwards, the effects of geometrical structure of the discrete rigid plate on the convergence is investigated. The geometries of the discrete rigid plates with an edge fillet used in the 2.5 mm and 15 mm crack analysis are shown in Figure 5.3.

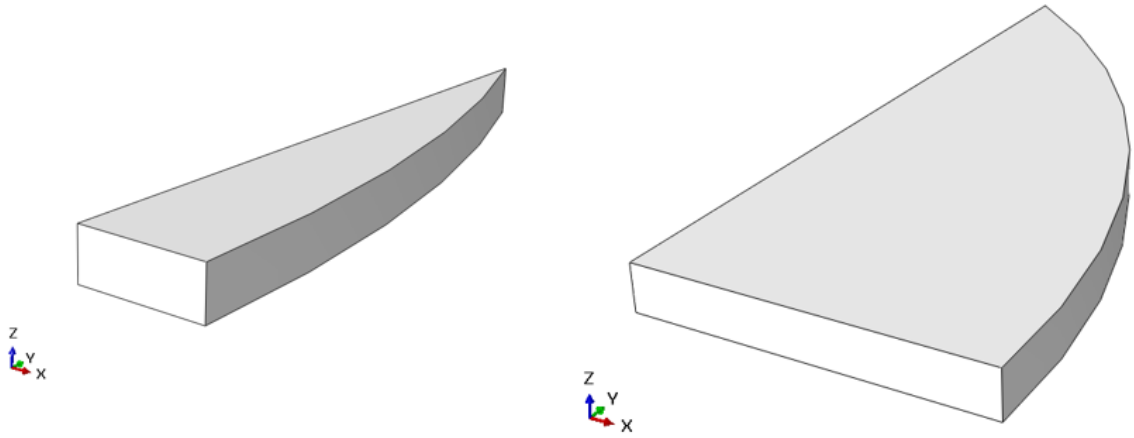


Figure 5.2. The geometries of the discrete rigid plates used in the 2.5 mm (left) and 15 mm stationary cracks.

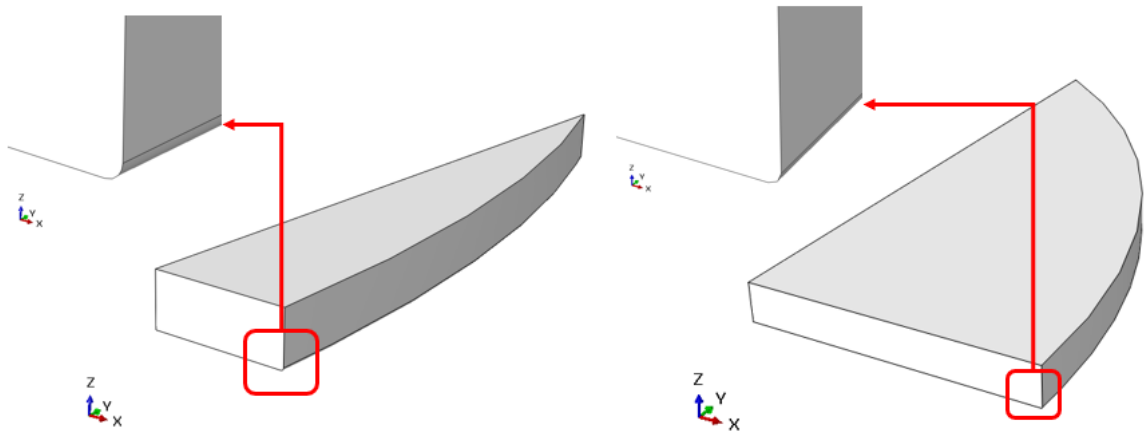


Figure 5.3. The geometries of the discrete rigid plates with an edge fillet used in the 2.5 mm (left) and 15 mm crack analysis.

5.1.3. Boundary Conditions and Loading

Discrete rigid body that represents steel plate is placed on the top surface of the rubber on which interface crack is placed. Symmetry boundary condition is applied on the surface which cuts the rubber in half symmetrically. A reference point is placed on the top surface of the rubber. Top surface of the rubber not containing crack is tied to this reference point and reference point is pinned, that is, displacement of this reference

point is not allowed. Another reference point is placed on the discrete rigid body and pinned so that movement of the discrete rigid plate is prevented. Displacements corresponding to 15% compression and 50% shear strains are applied on the bottom surface of the rubber. This load is applied in two steps. In the first step, only compression load is applied. In the second step, shear loading is added. Shear loading is applied in two different directions opposite to each other. Loading and boundary conditions for 2.5 mm and 15 mm crack analysis are shown in Figure 5.4 and Figure 5.5, respectively.

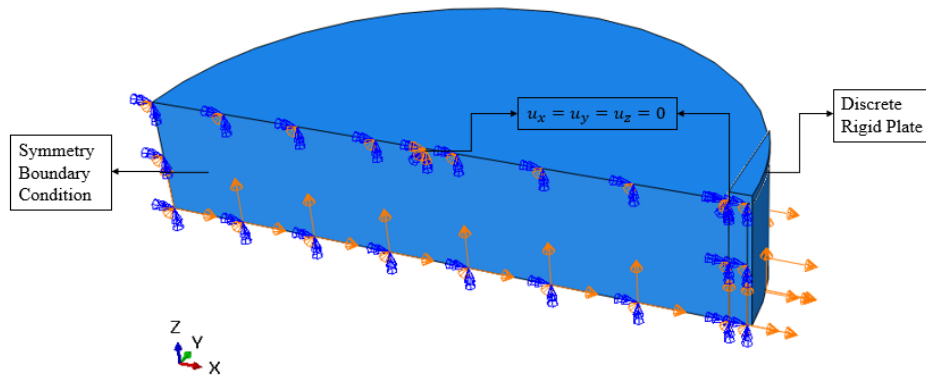


Figure 5.4. Boundary conditions and loading applied on the rubber and discrete rigid body for 2.5 mm stationary crack analysis.

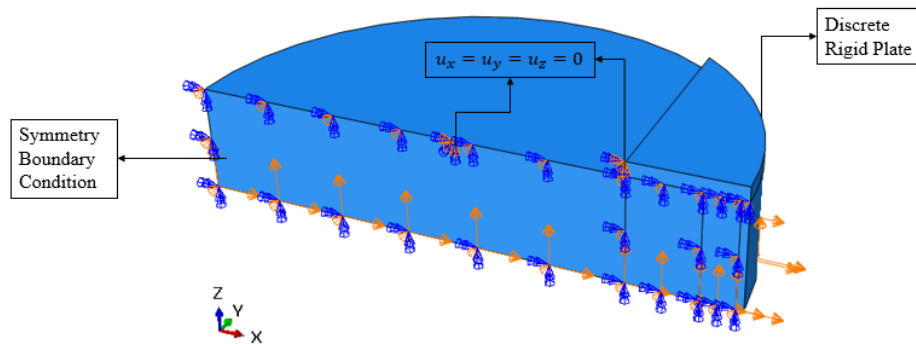


Figure 5.5. Boundary conditions and loading applied on the rubber and discrete rigid body for 15 mm stationary crack analysis.

5.1.4. Contact Interactions

Contact interaction between the discrete rigid plate surface and top surface of the rubber pad is defined. Normal and tangential contact properties used in the analysis are shown in Table 5.1. Penalty method is used for friction formulation. The effect of coefficient of friction values on the convergence of the problem is investigated.

Table 5.1. Interaction properties between discrete rigid plate and crack surface.

Normal Behaviour	Tangential Behaviour (Friction Formulation: Penalty) Coefficient of Friction
Hard Contact	0.35
	0.30
	0.25

5.2. Bearing with a Short Bondline Crack

Material model, geometry, boundary conditions, and contact properties mentioned in the previous sections are used for the 2.5 mm stationary crack analysis. The effects of the coefficient of friction and fillet radius on the convergence of the finite element analysis are investigated. 15% compression and 50% shear loading are applied on the rubber. Convergence for the strain values are presented for different coefficient of friction values and fillet radii.

5.2.1. Mesh Structure of the Discrete Rigid Plate

Mesh applied on the discrete rigid body consists of linear quadrilateral elements of type 4-node 3-D bilinear rigid quadrilateral (R3D4) and linear triangular elements of type 3-node 3-D bilinear rigid triangular (R3D3) elements. Mesh structure and the number of elements changed depending on whether there is an edge fillet or not.

For the case without fillet, 898 R3D4 and 6 R3D3 elements are used. The corresponding mesh structure of the discrete plate is shown in Figure 5.6.

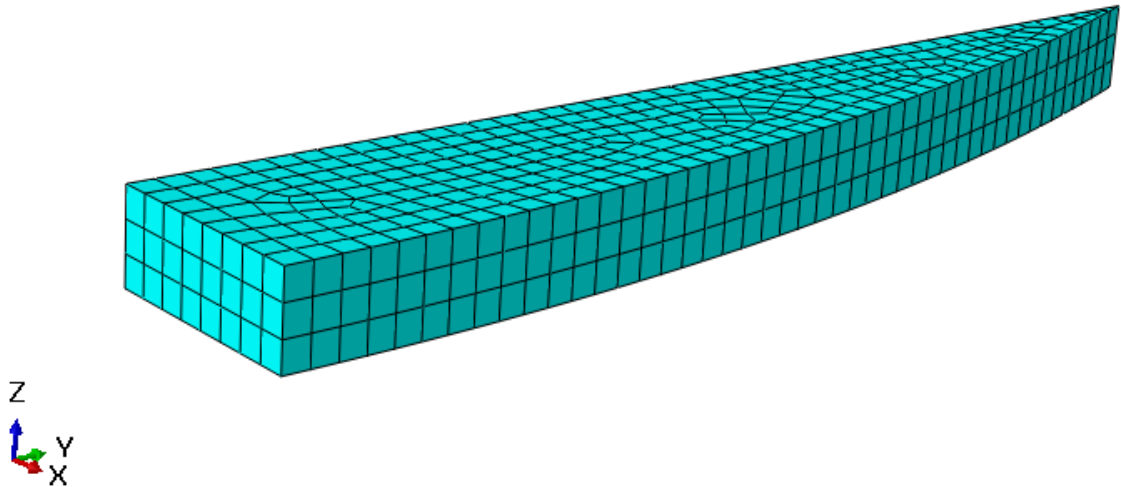


Figure 5.6. Mesh structure of the discrete rigid plate used for the 2.5 mm crack analysis (not containing fillet).

The mesh structures of the discrete rigid plate containing 0.05 mm and 0.1 mm fillet are shown in Figure 5.7.

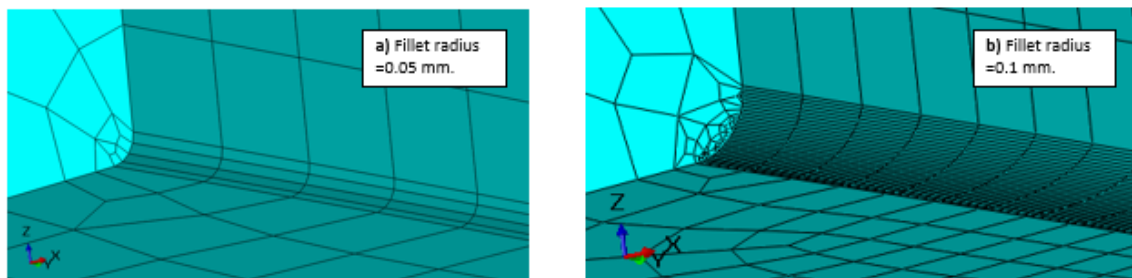


Figure 5.7. (a) Mesh structure of the discrete rigid plate containing 0.05 mm fillet (b) mesh structure of the discrete rigid plate containing 0.1 mm fillet for the 2.5 mm crack analysis.

5.2.2. Mesh Structure of the Rubber Pad

Mesh applied on the rubber pad consists of 8-node linear brick, hybrid, constant pressure, reduced integration, hourglass control (C3D8RH) elements. Generally, quadratic shape functions provide more accurate deformed shapes and prevent element distortions which may result in convergence problems for the large deformation analysis. On the other hand, high number of second order elements increases the computational time drastically. In this study, first order hybrid elements are used due to limitations of computational tools.

For each crack size a new mesh is constructed. Therefore, the number of elements and nodes are changed for each model. To be able to obtain good aspect ratios for the elements near the crack, partition is made on the top surface of the rubber as shown in Figure 5.9. Additionally, near the crack surface and crack front area, finer mesh structure is used since accuracy of the J integral value depends strongly on the quality of the mesh near the crack front. In the remainder of the rubber pad, course mesh is used. The mesh structure of the model with 2.5 mm crack consists of 8019 elements and is illustrated in Figure 5.8.

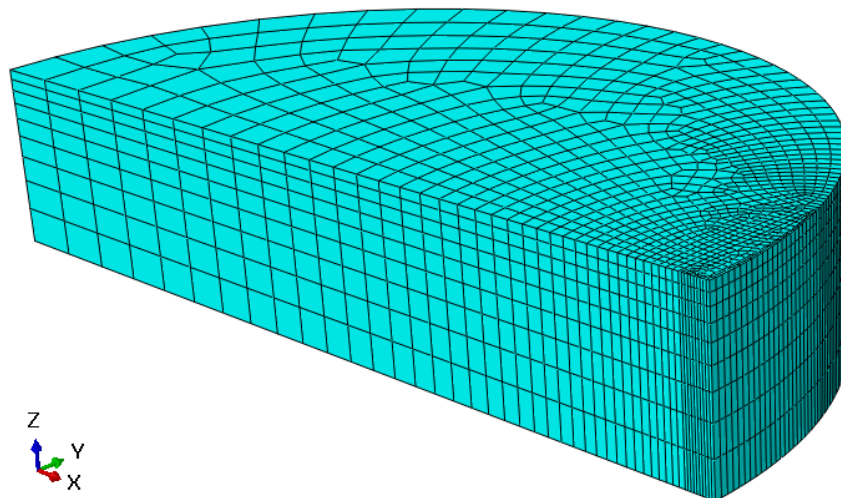


Figure 5.8. Mesh structure of the rubber pad for 2.5 mm interface crack.

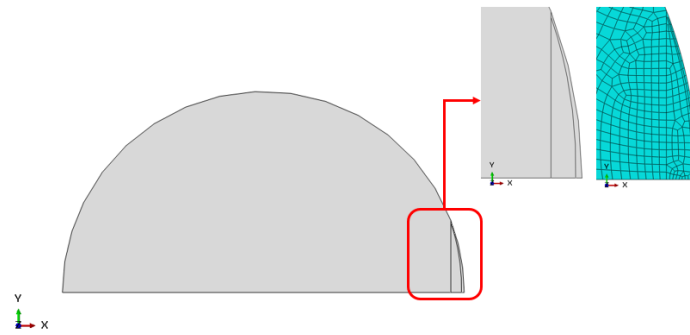


Figure 5.9. Partition on the top surface of the rubber and mesh structure near the edge.

The effect of mesh structure and element size on the convergence is investigated for 2.5 mm interface crack and is presented in Appendix A.

5.2.3. Results

Fillet radii having length of 0.05 mm and 0.1 mm and coefficient of friction values of 0.25, 0.30 and 0.35 are studied. The converged compression and shear strain values are given in Table 5.2.

Table 5.2. Compression and shear strains obtained for different coefficient of friction and fillet radius values for 2.5 mm crack analysis.

Coefficient of friction value	Fillet radius (<i>mm</i>)	Compression strain obtained (%)	Shear strain obtained (%)
0.25	0.05	10.04	-
0.30	0.05	15.00	50
0.35	0.05	15.00	50
0.25	0.1	0.25	-
0.30	0.1	0.9	-
0.35	0.1	0.75	-

It is seen that the maximum convergence is obtained for the coefficient of friction value of 0.30, 0.35 and fillet radius of 0.05 mm. It is also observed that there is a big difference between the converged compression strains of 0.05 mm fillet and 0.1 mm fillet. The deformed shapes for the models with 0.1 mm and 0.05 mm fillet radii are given in Figure 5.10.

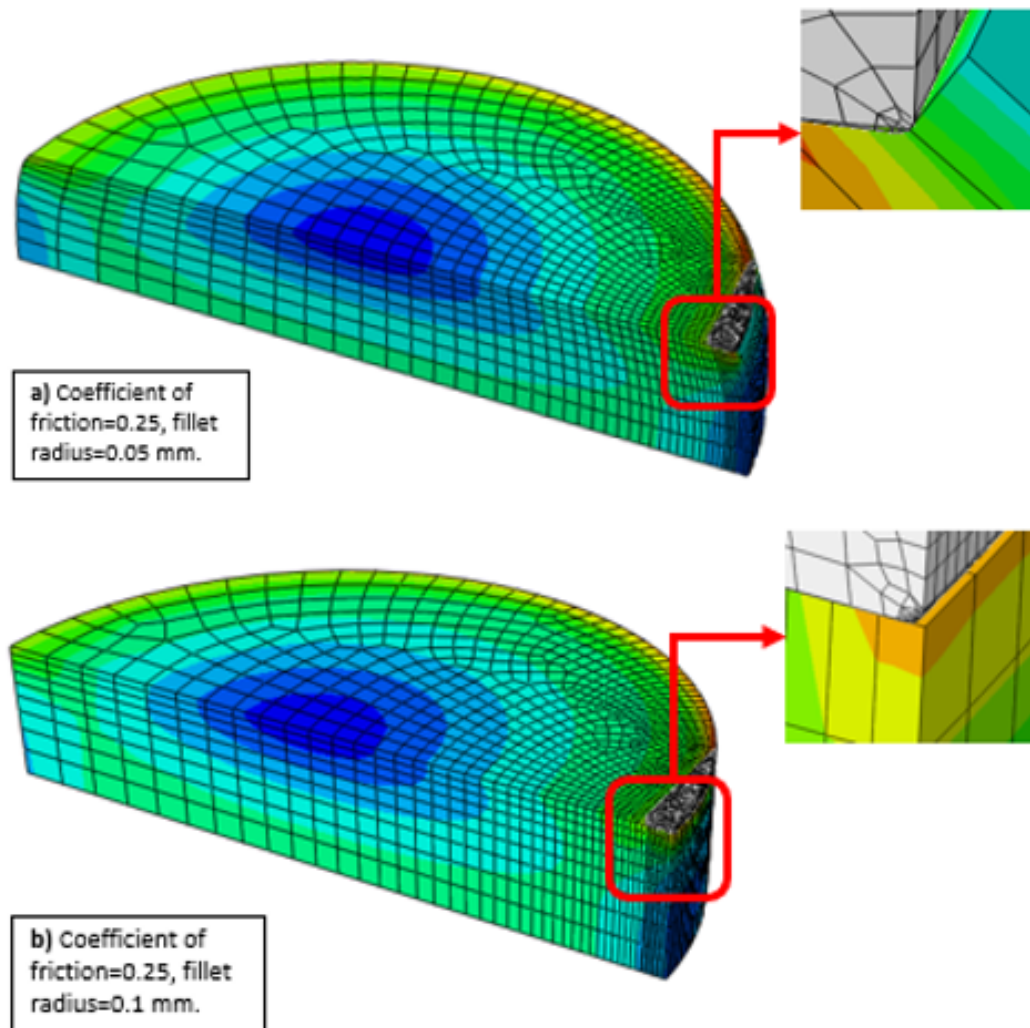


Figure 5.10. Comparison of the deformed shapes: (a) deformed shape for 0.25 coefficient of friction and 0.05 mm fillet radius (0.25% compression strain is obtained) (b) deformed shape for 0.25 coefficient of friction and 0.1 mm fillet radius (10.04% compression strain is obtained).

In the finite element model the rigid surface is selected as the master and the rubber surface as the slave surface. Generally, finer mesh is required on the slave surface so that the nodes are properly connected to the nodes on the master surface. For models with fillet, element size on the fillets becomes very fine as fillet radius gets smaller. However, due to the lack of powerful computational tools, element sizes on the crack surface remained larger than the element sizes on the fillet surfaces. Consequently, nodes were not well connected, and resulted in convergence problems. As can be seen in Figure 5.10, there are more nodes on the 0.1 mm fillet surface than the 0.05 mm case, consequently, it is more difficult for the software to connect the nodes on the rubber to the nodes on the rigid plate for 0.1 mm fillet than the 0.05 mm fillet. As a result of this, 0.25% compression is obtained for the 0.01 mm fillet whereas 10.04% compression is obtained for 0.05 mm crack. Further detail about the mesh is given in Appendix A.

Convergence also depends on the value of the coefficient of friction applied between the discrete rigid plate and crack surface of the rubber. As can be seen in Table 5.2, for the 0.05 mm fillet radius, when the coefficient of friction value is equal to 0.25, full convergence is not obtained (10.04%), on the other hand, for the values of the coefficient of friction of 0.30 and 0.35, full convergence is achieved. The reason of this is because when the value of the coefficient of friction decreases, displacement of the elements and nodes on the crack surface sweeping the fillet surface upon loading tends to increase. Due to element distortions and nodal connections between crack surface and discrete rigid plate, convergence stops. The deformed shapes of the rubber for the coefficient of friction values of 0.25 and 0.35 is given in Figure 5.11.

For the 0.1 mm fillet case, at any coefficient of friction value, convergence is achieved for very small amount of compression strain. It is realized that there is a fluctuation of the results regarding the compression strain obtained by increasing the value of the coefficient of friction. The reason of this fluctuation is probably due to the poor connection of the nodes between rubber and discrete rigid plate.

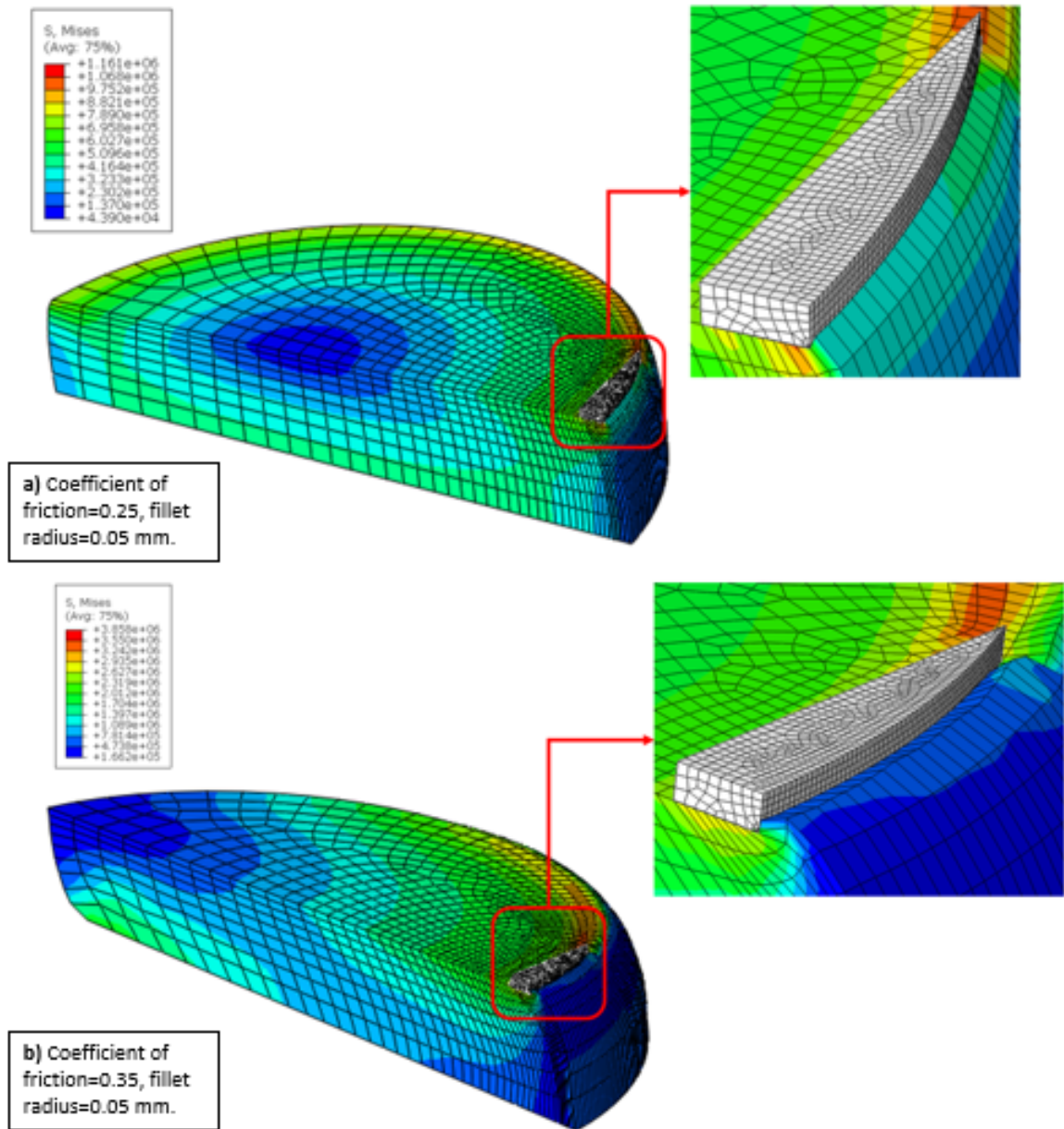


Figure 5.11. Comparison of the deformed shapes: (a) deformed shape for 0.25 coefficient of friction, 0.05 mm fillet radius (10.04% compression strain is obtained)
 (b) deformed shape for 0.35 coefficient of friction, 0.05 mm fillet radius (15% compression and 50% shear strains are obtained).

5.3. Bearing with a Long Bondline Crack

Same material model, boundary conditions, loading and contact properties used for the 2.5 mm interface crack analysis are used for the 15 mm interface crack analysis. In this section, the effects of the fillet radius and the coefficient of friction applied between the rubber and discrete rigid plate's surface on the convergence for 15 mm stationary interface crack are investigated.

5.3.1. Mesh Structure of the Discrete Rigid Plate

Mesh structure for 15 mm stationary interface crack analysis contains 3672 elements. The same type of elements in Section 5.2.1 are used. The structure of the mesh applied on the geometry is shown in Figure 5.12. The number of the elements applied on the discrete rigid plate changed depending on the fillet radius. The course mesh structures on the 0.05 mm and 0.1 mm fillets are shown in Figure 5.13.

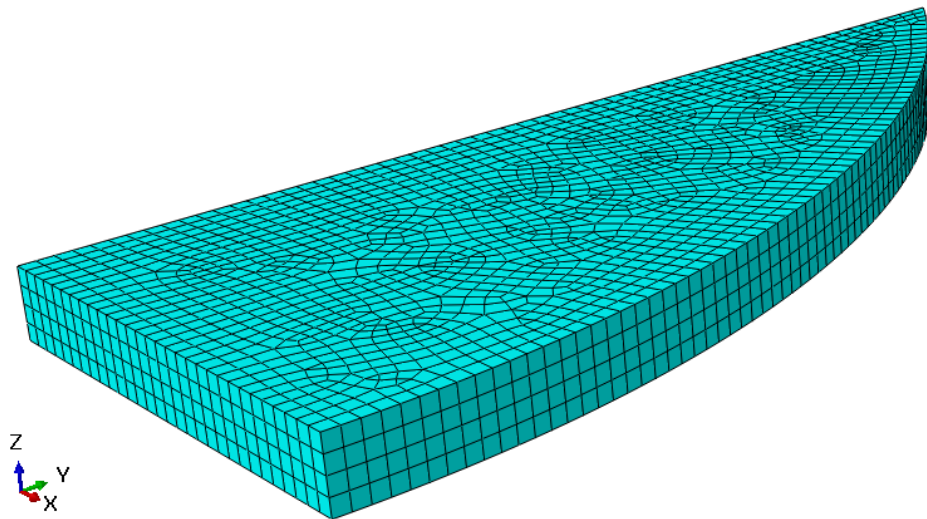


Figure 5.12. Mesh structure of the discrete rigid plate for 15 mm interface crack (not containing fillet).

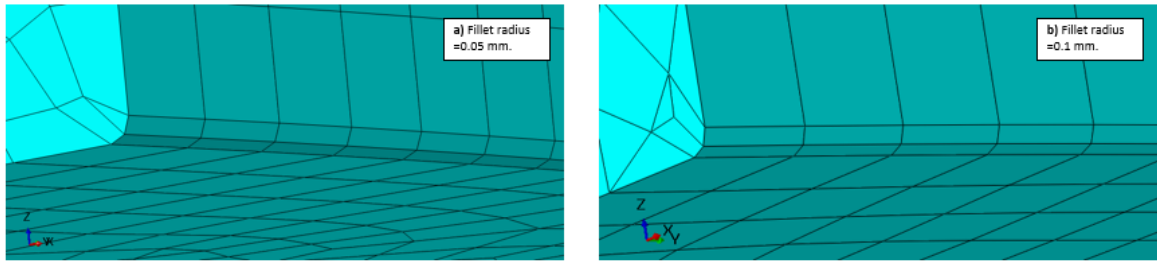


Figure 5.13. (a) Mesh structure of the discrete rigid plate containing 0.05 mm fillet
 (b) mesh structure of the discrete rigid plate containing 0.1 mm fillet for the 15 mm
 crack analysis.

5.3.2. Mesh Structure of the Rubber Pad

In order to prevent convergence problems due to arbitrary element shapes around the circular arc, well structured mesh is used by means of the partition on the crack surface as shown in Figure 5.14.

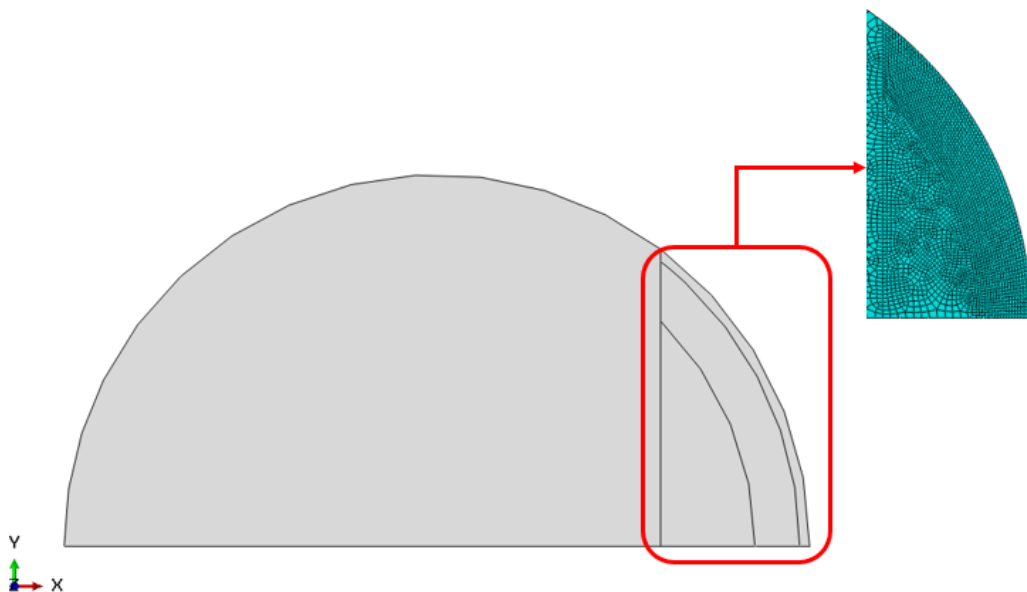


Figure 5.14. Partition on the top surface of the rubber and mesh structure on the 15
 mm crack surface.

In order to achieve better representation of the deformed shape, finer mesh structure is constructed around the 15 mm crack. Furthermore, finer mesh is used around the crack front to obtain more accurate J integral values. To reduce the run time, very course mesh is used for the rest of the rubber. 22008 linear hexahedral elements of type 8-node linear brick, hybrid, constant pressure, reduced integration, hourglass control (C3D8RH) are used. The mesh structure used for the 15 mm crack analysis is presented in Figure 5.15. To analyze the effect of the mesh on the convergence of the problem, finer mesh is constructed as seen in Figure 5.16 for a 0.1 mm fillet and 0.25 coefficient of friction. Mesh consists of 145486 linear hexahedral elements of type C3D8RH.

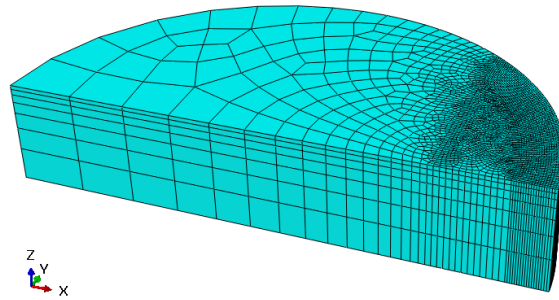


Figure 5.15. Mesh structure applied on the rubber for 15 mm interface crack analysis.

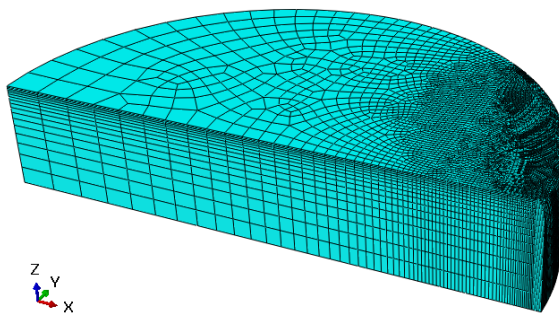


Figure 5.16. Fine mesh structure applied on the rubber for 15 mm interface crack analysis.

5.3.3. Results

The effects of the various coefficient of friction and fillet radius values on the convergence of the problem are presented in Table 5.3. As can be seen in Table 5.3, limited convergence is achieved for the selected fillets and coefficient of friction values. The convergence stops in the compression loading step, so no shear strain was applied. Maximum convergence (7.43% compression) is obtained for 0.1 mm fillet and coefficient of friction value of 0.25.

Table 5.3. Comparison and shear strains obtained for different coefficient of friction and fillet radius values for 15 mm crack analysis.

Coefficient of friction value	Fillet radius (<i>mm</i>)	Compression strain obtained (%)	Shear strain obtained (%)
0.25	0.05	5.72	-
0.30	0.05	5.59	-
0.35	0.05	5.36	-
0.25	0.1	7.43	-
0.30	0.1	7.34	-
0.35	0.1	6.62	-

Deformed shapes of the rubber containing 15 mm interface crack and with 0.05 mm and 0.1 mm fillets for 0.30 coefficient of friction are shown in Figure 5.17 and Figure 5.18. Contrary to the results obtained from the 2.5 mm crack analysis, there is no significant difference in the compression strains obtained between 0.05 mm and 0.1 mm fillets. Convergence slightly improved for the 0.1 mm fillet. For both fillet cases, increase in the coefficient of friction resulted in decrease in the converged compression loading unlike the 2.5 mm crack model. In the model with 15 mm crack, fewer number of elements and nodes are constructed as compared to 2.5 mm crack model. When the coefficient of friction value is decreased, element faces on the rubber sweep the element faces on the fillet more. As explained in Section 5.2.3, due to the element sizes on

the rubber, connection of the nodes between rubber and rigid plate were problematic. It is more difficult to obtain better converged compression loading if the value of the coefficient of friction is decreased, thereby, more deformation of the crack surface of the rubber is obtained resulting in more convergence problems.

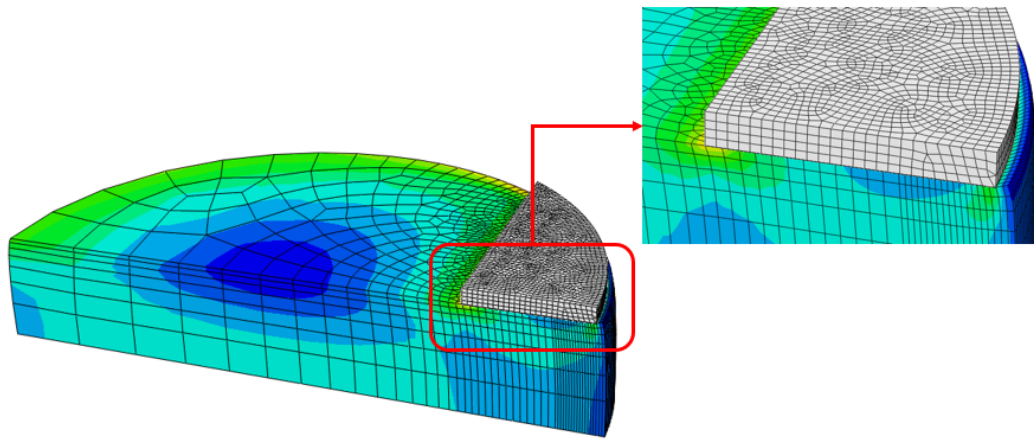


Figure 5.17. Deformed shape of the rubber pad with 15 mm crack subjected to compression and shear (coefficient of friction=0.3, fillet radius=0.05 mm and compression strain obtained=5.59%).

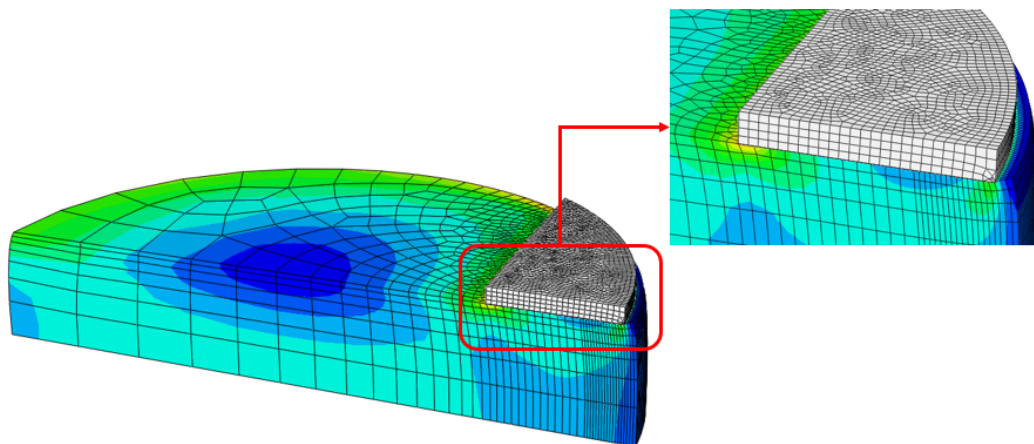


Figure 5.18. Deformed shape of the rubber pad with 15 mm crack subjected to compression and shear (coefficient of friction=0.3, fillet radius=0.1 mm and compression strain obtained=7.34%).

A finer mesh for 0.1 mm fillet radius and 0.25 coefficient of friction values was constructed. As can be seen in Figure 5.19, finer mesh model results in further convergence (11.71% compression strain) than the course mesh (7.43% compression strain). It can be concluded that mesh structure has a major role on the interface crack analysis for elastomeric isolation bearings. Finer mesh structures, thus, advanced computational tools are required for the accuracy of the interface crack analysis. However, due to the cost of using high number of elements or elements with second order shape functions, this model is used just for demonstration purposes to emphasize the importance of using finer mesh structures on the problem convergence.

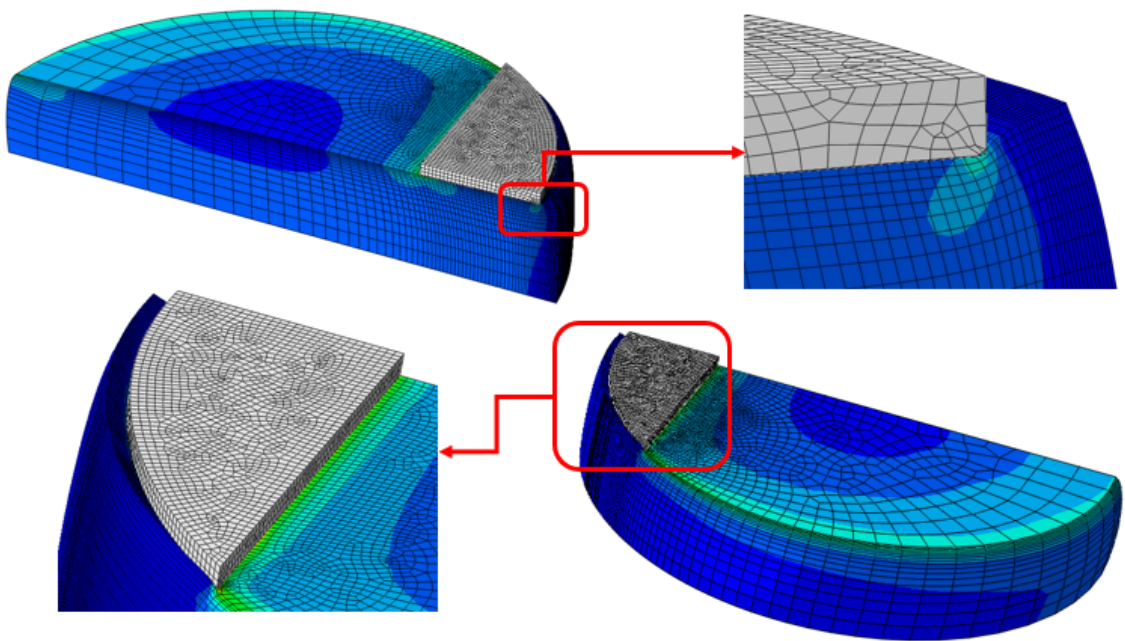


Figure 5.19. For the fine mesh, deformed shapes of the rubber pad with 15 mm crack subjected to compression and shear for 15 mm crack analysis (coefficient of friction=0.25, fillet radius=0.1 mm and compression strain obtained=11.71%).

5.4. J Integral Comparison between Two Interface Cracks

The purpose of this section is to compare the values of the J integrals obtained from 2.5 mm and 15 mm interface crack analysis presented in Section 5.2 and Section 5.3, respectively. Rubber is subjected to 5% compression and 50% shear strains. Based on the results presented in Table 5.2 and Table 5.3, 0.05 mm fillet and 0.30 coefficient of friction is used. The mesh structures shown in Figure 5.8 and Figure 5.15, are used for this model as well. The mesh structures of the discrete rigid plate with 0.05 mm fillet used for 2.5 mm and 15 mm crack analysis are used. Full convergence is obtained for both short crack and long interface crack models. The deformed shapes are shown in Figure 5.20 and Figure 5.21.

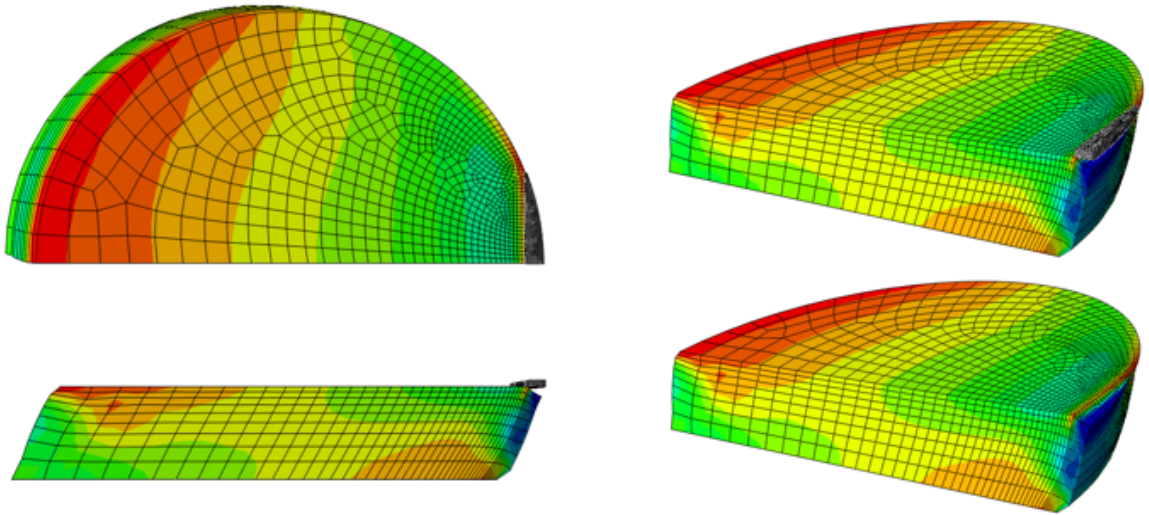


Figure 5.20. Deformed shapes of the rubber subjected to 5% compression and 50% shear for 2.5 mm interface crack analysis (coefficient of friction=0.30 and fillet radius=0.05 mm).

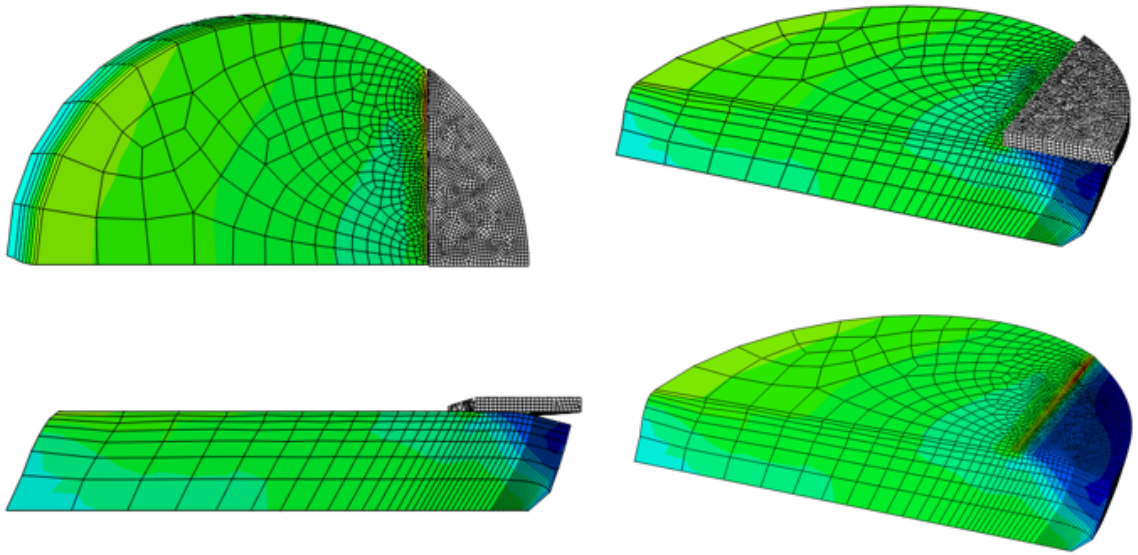


Figure 5.21. Deformed shapes of the rubber subjected to 5% compression and 50% shear for 15 mm interface crack analysis (coefficient of friction=0.30 and fillet radius=0.05 mm).

In Figures 5.22 and 5.23, J integral values are shown for 2.5 mm and 15 mm cracks, respectively. In the first step (From time=0 sec. to 1 sec.), as compression load is applied to the rubber, increase in the J integral values for both of the cracks is observed. Afterwards, together with the compression, shear load is applied in the second step (From time=1 sec. to 2 sec.). In this step, for both bondline cracks, the value of the J integral decreases at first. After a certain time period, the J integral value starts rising again. At the beginning of the shear load, rubber is in contact with the discrete rigid plate due to the deformation which is originated from the compression loading. This is the reason of the decrease in J integral value. J integral value starts increasing when crack starts to open. Comparison of Figures 5.22 and 5.23 shows that the predicted J integral values for compression as well as combined loading, decrease as the crack size increases. This result is expected and was also observed in 2D crack model presented in Section 4.3. It can be, therefore, concluded that the analysis presented in this section gives the correct trend of J values, although further mesh study is needed to increase confidence in the calculated J values.

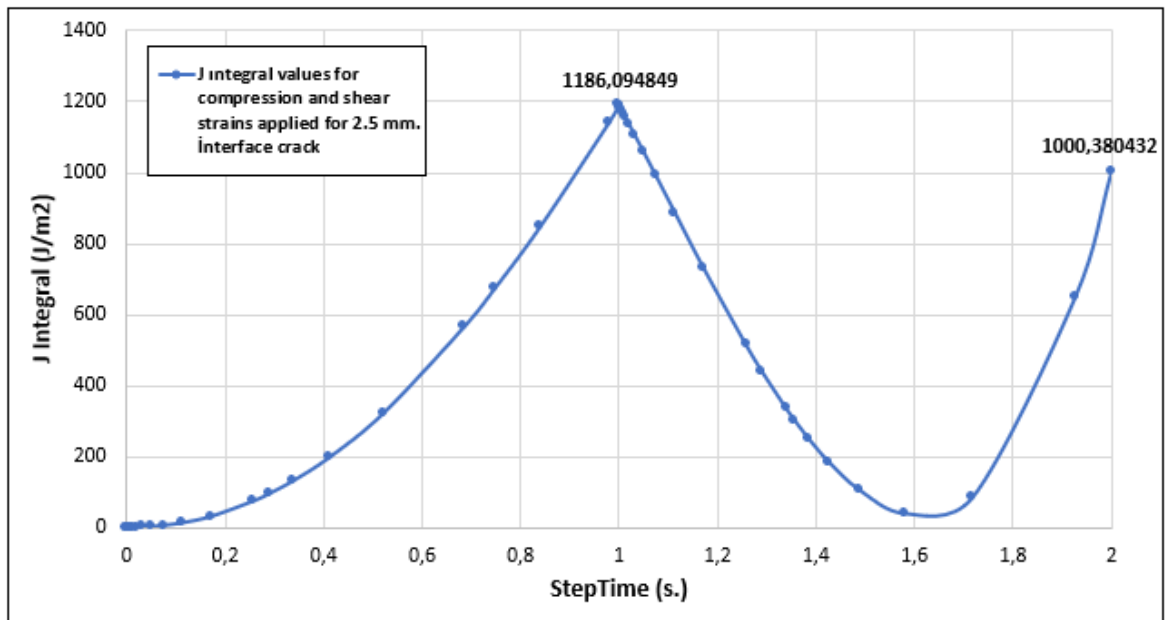


Figure 5.22. J Integral for short bondline crack.

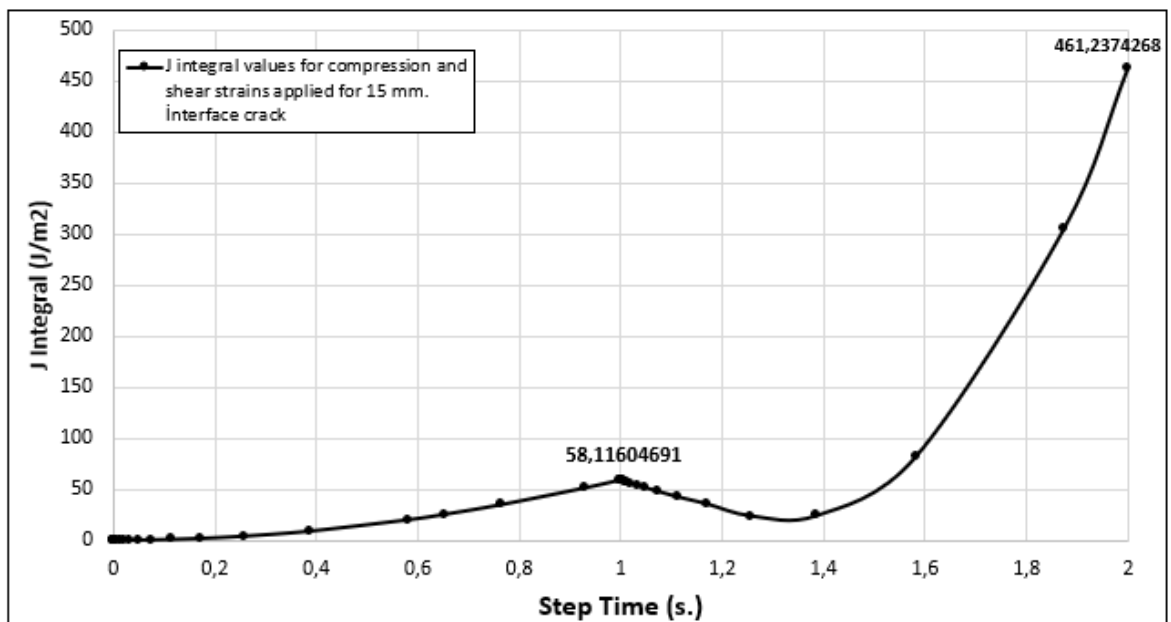


Figure 5.23. J Integral for long bondline crack.

6. CONCLUSION

In this thesis, XFEM and FEM models (2D and 3D) of a benchmark problem related to crack propagation analysis in a single-edge notch specimen, 2D crack modeling in an elastomeric isolation bearing under compression and 3D crack modeling in an elastomeric isolation bearing under compression and shear were constructed.

The benchmark problem allowed evaluation of the XFEM capabilities to model crack propagation. The comparison of FEM and XFEM results showed good agreement of the strain energy values. In 2D and 3D analyses the difference was found as 2.7% and 1.9%, respectively. The shortcoming of XFEM was determined as the lack of J integral calculations during crack propagation. To overcome this, the dissipated energy was explored as the quantity from which to extract the J integral. For small crack advances, dissipated energy values obtained from the XFEM were found to agree with those based on J integral calculated from FEM. However, due to the time inefficiency of the procedure it was decided to continue the crack modeling in isolation bearing with the conventional FEM.

Two dimensional analysis of a circular isolation bearing made out of filled natural rubber was concerned with bondline crack modeling under 35% compression loading. The modeling of the rigid end plates and the coefficient of friction used in contact modeling were found to be important parameters in the full convergence of this numerically challenging problem. In particular, the geometry of the rigid plate and the radius of the fillet introduced in the plate were optimized for accuracy and computational time. The analyses were carried out for both bonded and unbonded boundary conditions. The predictions for reaction forces and J integral values for various crack lengths showed good agreement with previous analyses and test data.

Three dimensional analysis of a circular isolation bearing made out of filled natural rubber was concerned with bondline crack modeling under combined compression

and shear loading, 15% and 50% strains, respectively. Bonded boundary condition was modeled and the most efficient rigid plate geometry as determined in two dimensional analysis was used. Short and long cracks showed different convergence behaviors. For a short crack under compression, full convergence was possible for a rigid plate with fillet radius much smaller than the one determined in two dimensional analysis. For a long crack full convergence was not achieved. As a consequence comparison with previous data for 15% compression and 50% shear loading was not carried out. Nevertheless, evaluation of the J integral for the partial compression load and 50% shear strain showed the expected trend with respect to the crack size.

It was concluded that three dimensional crack modeling for compression loading is very demanding computationally and further investigation is needed to increase confidence in the accuracy of the predictions.

Because of the hyper-elastic and nearly incompressible behavior of rubber, complex loading conditions (large compression and shear strains), numerically challenging features (interface crack), the future focus of this study would be to conduct detailed mesh convergence study and explore second order shape functions. Another topic of interest would be to explore an efficient way of extracting J integral value from XFEM results.

Finally, if both material response and fatigue test data were available for an elastomeric isolation bearing, crack propagation analysis based on XFEM may be used for fatigue life estimation.

REFERENCES

1. Wang, S., Y. Yuan, P. Tan, H. Zhu and K. Luo, “Experimental Study on Mechanical Properties of Casting High-Capacity Polyurethane Elastomeric Bearings”, *Construction and Building Materials*, Vol. 265, p. 120725, 2020.
2. Kelly, J. M. and D. Konstantinidis, “Effect of Friction on Unbonded Elastomeric Bearings”, *Journal of Engineering Mechanics*, Vol. 135, pp. 953–960, 2009.
3. Zhong, H., W. Yuan, X. Dang and X. Deng “Seismic Performance of Composite Rubber Bearings for Highway Bridges: Bearing Test and Numerical Parametric Study”, *Engineering Structures*, Vol. 153, p. 113680, 2022.
4. Mohamedmeki, Z. M., F. J. Esmail and E. A. Ajeel, ”Fatigue Life Analysis of Laminated Elastomeric Bearing Pad”, *Materials Today: Proceedings*, Vol. 42, pp. 2361-2368, 2021.
5. Inc, S., “Abaqus Documentation 6.6” , 2014, [https:// classes. engineering. wustl. edu/](https://classes.engineering.wustl.edu/), accessed on November 21, 2015.
6. Park, S. J., M. S. Seo, “Interface Science and Composites”, Vol. 18, *Academic Press*, London, 2011.
7. Amin, A., S. Wiraguna, A. Bhuiyan and Y. Okui, “Hyperelasticity Model for Finite Element Analysis of Natural and High Damping Rubbers in Compression and Shear”, *Journal of Engineering Mechanics*, Vol. 132, No. 1, pp. 54–64, 2006.
8. Yurdabak, V. and Ş. Özüpek, “Explicit Solution Methods in Quasi-Static Analysis of Rubber-Like Materials”, *Rubber Chemistry and Technology*, Vol. 92, pp. 399–413, 2016.
9. Stevenson, A., J. Hawkes, J. Harris and P. Hansen, “Fatigue Life of Elastomeric

- Engineering Components under Biaxial Loading Using Finite Element Analysis”, *SAE International*, Warrendale, United States, 1998.
10. Charrier, P., E. Ostojka-Kuczynski, E. Verron, G. Marckmann, L. Gornet and G. Chagnon, “Theoretical and Numerical Limitations for the Simulation of Crack Propagation in Natural Rubber Components”, *3rd European Conference on Constitutive Models for Rubber (ECCMR)*, Vol. 3, London, United Kingdom, 2003.
 11. Cho, H. W. and J. S. Huang, “Crack Initiation and Propagation in Circular Rubber Bearings Subjected to Cyclic Compression”, *Journal of Applied Polymer Science*, Vol. 121, No. 3, pp. 1747–1756, 2011.
 12. Cho, H. W. and J. S. Huang, “Fatigue Life Prediction for Circular Rubber Bearings Subjected to Cyclic Compression”, *Journal of Applied Polymer Science*, Vol. 123, No.4, pp. 2194-2203, 2012.
 13. Özüpek, Ş. and Ç. Iyidiker, “Modeling Cracks in Nonlinear Viscoelastic Media Subjected to Thermal Loading”, *Journal of Propulsion and Power*, Vol. 33, No. 2, pp. 305-312, 2017.
 14. Gajewski, M., R. Szczerba and S. Jemiolo, “Modelling of Elastomeric Bearing with Application of Yeoh Hyperelastic Material Model”, *Procedia Engineering*, Vol. 111, pp. 220–227, 2015.
 15. Rice, J. R., “A Path Independent Integral and the Approximate Analysis of Strain Concentration by Notches and Cracks”, *Journal of Applied Mechanics*, pp. 379–386, 1968.
 16. Chen, M., H. Wang, H. Jin, X. Pan and Z. Jin, “Transient Thermal Shock Behavior Simulation of Porous Silicon Nitride Ceramics”, *Ceramics International*, Vol. 42, pp. 3130–3137, 2016.
 17. Johnson, A., N. Toso-Pentecôte and D. Schueler, ”Numerical Modelling of Impact

- and Damage Tolerance in Aerospace Composite Structures”, *Numerical Modelling of Failure in Advanced Composite Materials*, pp. 479-506, Elsevier, Amsterdam, 2015.
18. Wu, E. M., R. Reuter Jr, ”Crack Extension in Fiberglass Reinforced Plastics”, Illinois University at Urbana Department of Theoretical and Applied Mechanics, 1965.
 19. de Oliveira G´oes, R. C., J. T. P. de Castro and L. F. Martha, “3D Effects around Notch and Crack Tips”, *International Journal of Fatigue*, Vol. 62, pp. 159–170, 2014.

APPENDIX A: CONVERGENCE STUDY FOR THREE DIMENSIONAL MODEL (2.5 mm INTERFACE CRACK ANALYSIS)

The purpose is to conduct a mesh study to get a solution for the three dimensional interface crack problem for 15% compression and 50% shear strains with 2.5 mm interface crack. For all analyses, coefficient of friction value is set to 0.35. There is an edge fillet on the discrete rigid plate whose radius is 0.05 mm. 8-node linear brick, hybrid, constant pressure, reduced integration, hourglass control (C3D8RH) element type is used. Initially, number of elements is kept very low so as to investigate if the solution converges. Therefore, mesh is composed of only 5348 elements. Finer mesh structure around the crack front and crack surface is accomplished as it can be seen in Figure A.1. Solution convergence is obtained for the 15% compression loading. However, no convergence is obtained for the shear loading. The reason of this is because element size is so large that element at the edge of the rubber cannot deform around the edge fillet of the discrete rigid plate.

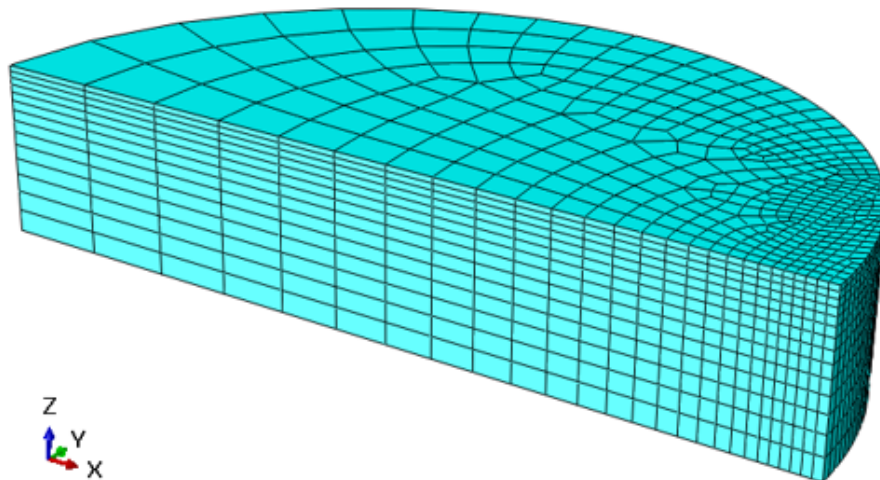


Figure A.1. Mesh structure consisting of 5348 elements.

Afterwards, total number of mesh is increased to 13446. Finer mesh is structured on the crack surface of the rubber as it is illustrated in Figure A.2. Convergence is obtained for 15% compression loading. However, convergence stops after reaching to 21.10% shear strain. Further mesh development is achieved by partitioning the crack surface so that element shapes are relatively well structured near the edge of the discrete rigid plate. Partition and mesh structure consisting of 10692 elements are shown in Figure A.3. In this case, only 14.38% compression strain is obtained.

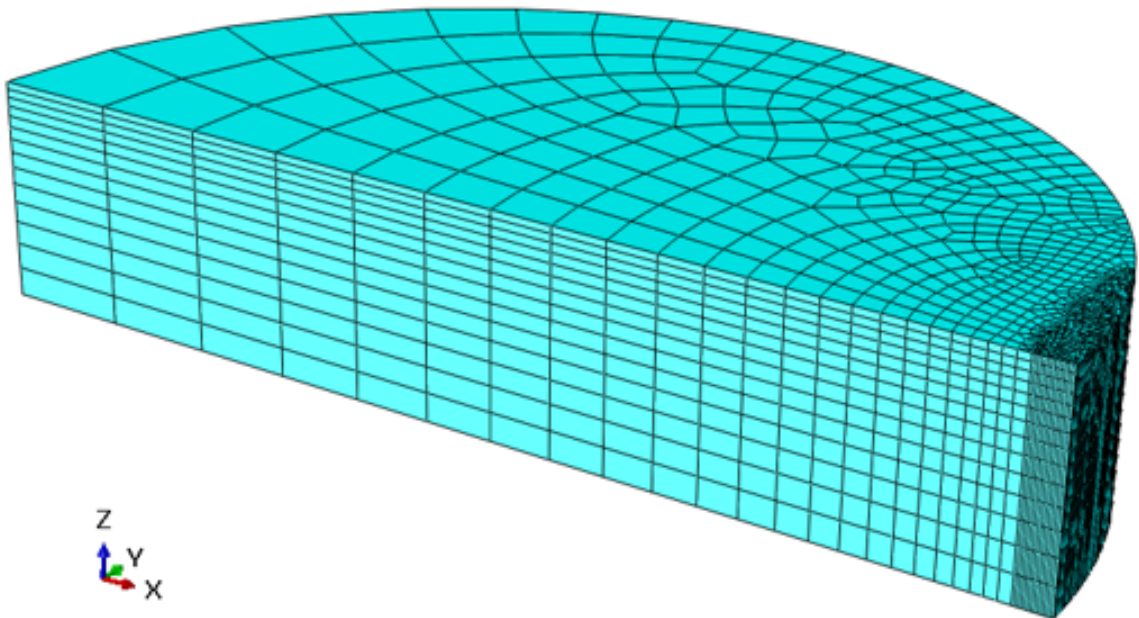


Figure A.2. Mesh structure consisting of 134462 elements.

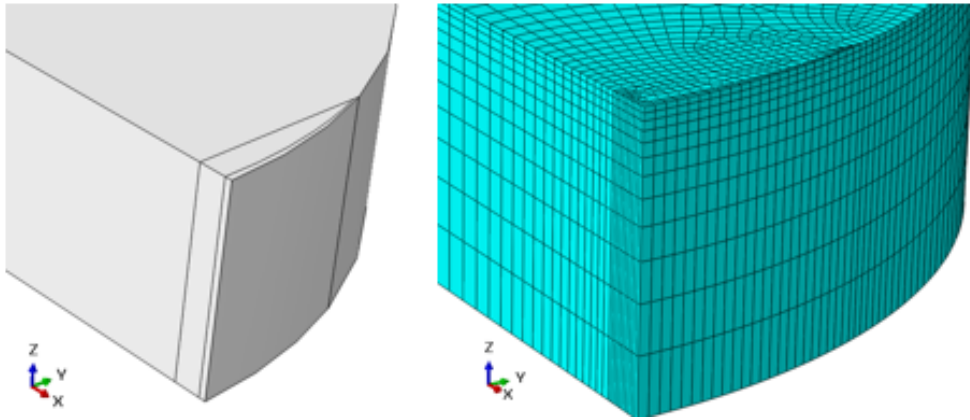


Figure A.3. Mesh structure consisting of 10692 elements.

Finally, the partition shown in Figure A.3 is used. The mesh based on this partition had 8019 elements and is shown in Figure A.4. Convergence was achieved for 15% compression and 50% shear strains.

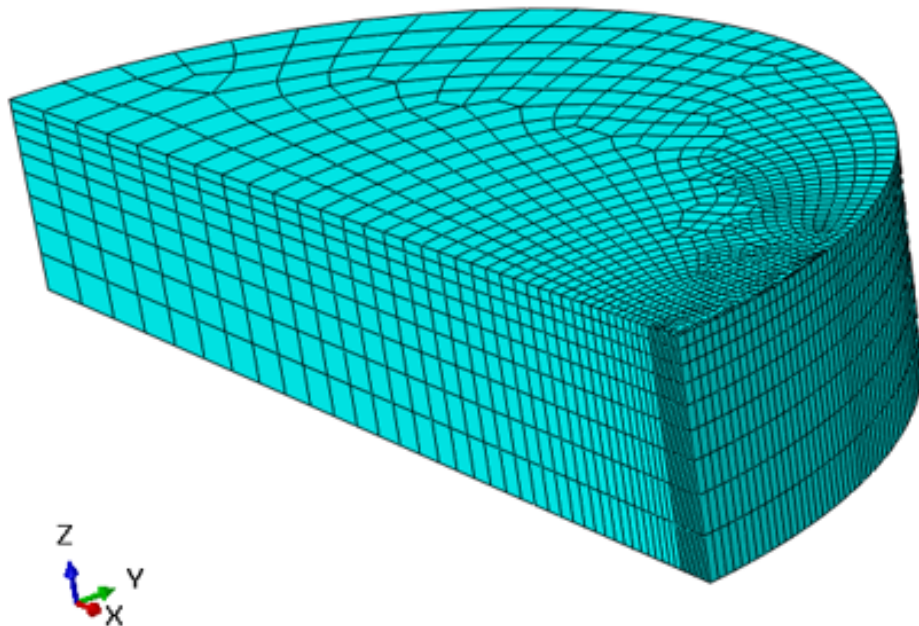


Figure A.4. Mesh structure consisting of 8019 elements.

APPENDIX B: ELSEVIER LICENSE NUMBER

5455320950504

ELSEVIER LICENSE TERMS AND CONDITIONS

Jan 01, 2023

This Agreement between Boğaziçi University – Emirhan Tıkız ("You") and Elsevier ("Elsevier") consists of your license details and the terms and conditions provided by Elsevier and Copyright Clearance Center.

License Number	5455320950504
License date	Dec 24, 2022
Licensed Content Publisher	Elsevier
Licensed Content Publication	Construction and Building Materials
Licensed Content Title	Experimental study on mechanical properties of casting high-capacity polyurethane elastomeric bearings
Licensed Content Author	Siqi Wang, Yong Yuan, Ping Tan, Hongping Zhu, Kaitao Luo
Licensed Content Date	Dec 30, 2020
Licensed Content Volume	265
Licensed Content Issue	n/a
Licensed Content Pages	1
Start Page	120725
End Page	0
Type of Use	reuse in a thesis/dissertation
Portion	figures/tables/illustrations
Number of figures/tables/illustrations	2
Format	both print and electronic
Are you the author of this Elsevier article?	No
Will you be translating?	Yes, including English rights
Number of translations	2
Title	CRACK PROPAGATION ANALYSIS IN ELASTOMERIC RUBBER BEARINGS
Institution name	Boğaziçi University
Expected presentation date	Jan 2023

Figure B.1. Elsevier license of Ref.[1] for Figure 1.1.

APPENDIX C: ELSEVIER LICENSE NUMBER

5455540009238

ELSEVIER LICENSE TERMS AND CONDITIONS

Jan 01, 2023

This Agreement between Boğaziçi University – Emirhan Tıkız ("You") and Elsevier ("Elsevier") consists of your license details and the terms and conditions provided by Elsevier and Copyright Clearance Center.

License Number	5455540009238
License date	Dec 24, 2022
Licensed Content Publisher	Elsevier
Licensed Content Publication	Engineering Structures
Licensed Content Title	Seismic performance of composite rubber bearings for highway bridges: Bearing test and numerical parametric study
Licensed Content Author	Haiqiang Zhong,Wancheng Yuan,Xinzhi Dang,Xiaowei Deng
Licensed Content Date	Feb 15, 2022
Licensed Content Volume	253
Licensed Content Issue	n/a
Licensed Content Pages	1
Start Page	113680
End Page	0
Type of Use	reuse in a thesis/dissertation
Portion	figures/tables/illustrations
Number of figures/tables/illustrations	1
Format	both print and electronic
Are you the author of this Elsevier article?	No
Will you be translating?	Yes, including English rights
Number of translations	2
Title	CRACK PROPAGATION ANALYSIS IN ELASTOMERIC RUBBER BEARINGS
Institution name	Boğaziçi University
Expected presentation date	Jan 2023

Figure C.1. Elsevier license of Ref.[3] for Figure 1.2.

APPENDIX D: ELSEVIER LICENSE NUMBER

5455530640334

ELSEVIER LICENSE TERMS AND CONDITIONS

Jan 01, 2023

This Agreement between Boğaziçi University – Emirhan Tıkız ("You") and Elsevier ("Elsevier") consists of your license details and the terms and conditions provided by Elsevier and Copyright Clearance Center.

License Number	5455540009238
License date	Dec 24, 2022
Licensed Content Publisher	Elsevier
Licensed Content Publication	Engineering Structures
Licensed Content Title	Seismic performance of composite rubber bearings for highway bridges: Bearing test and numerical parametric study
Licensed Content Author	Haiqiang Zhong,Wancheng Yuan,Xinzhi Dang,Xiaowei Deng
Licensed Content Date	Feb 15, 2022
Licensed Content Volume	253
Licensed Content Issue	n/a
Licensed Content Pages	1
Start Page	113680
End Page	0
Type of Use	reuse in a thesis/dissertation
Portion	figures/tables/illustrations
Number of figures/tables/illustrations	1
Format	both print and electronic
Are you the author of this Elsevier article?	No
Will you be translating?	Yes, including English rights
Number of translations	2
Title	CRACK PROPAGATION ANALYSIS IN ELASTOMERIC RUBBER BEARINGS
Institution name	Boğaziçi University
Expected presentation date	Jan 2023

Figure D.1. Elsevier license of Ref.[4] for Figure 1.3.